NAVAL POSTGRADUATE SCHOOL

MONTEREY, CALIFORNIA

THESIS

DEVELOPMENT OF A WIDEBAND THZ FOCAL PLANE ARRAY FOR SPACE APPLICATIONS

by

Anish H. Bhatt

June 2020

Thesis Advisor: Fabio D. Durante Pereira Alves
Co-Advisor: Wenschel D. Lan

THIS PAGE INTENTIONALLY LEFT BLANK

REPORT DOCUMENTATION PAGE			*Form Approved OMB No. 0704-0188*

1. AGENCY USE ONLY *(Leave blank)*	**2. REPORT DATE** June 2020	**3. REPORT TYPE AND DATES COVERED** Master's thesis

4. TITLE AND SUBTITLE DEVELOPMENT OF A WIDEBAND THZ FOCAL PLANE ARRAY FOR SPACE APPLICATIONS	**5. FUNDING NUMBERS**
6. AUTHOR(S) Anish H. Bhatt	
7. PERFORMING ORGANIZATION NAME(S) AND ADDRESS(ES) Naval Postgraduate School Monterey, CA 93943-5000	**8. PERFORMING ORGANIZATION REPORT NUMBER**
9. SPONSORING / MONITORING AGENCY NAME(S) AND ADDRESS(ES) N/A	**10. SPONSORING / MONITORING AGENCY REPORT NUMBER**

11. SUPPLEMENTARY NOTES The views expressed in this thesis are those of the author and do not reflect the official policy or position of the Department of Defense or the U.S. Government.

12a. DISTRIBUTION / AVAILABILITY STATEMENT Approved for public release. Distribution is unlimited.	**12b. DISTRIBUTION CODE** A

13. ABSTRACT (maximum 200 words)

This thesis builds upon the research being conducted in the Sensor Research Laboratory in the Physics Department at the Naval Postgraduate School (NPS) in collaboration with the Space Systems Academic Group. The goal is to contribute to the development of MEMS terahertz (THz) to infrared (IR) converters for real-time imaging, with potential applications to the space environment. The NPS MEMS THz-to-IR converters are typically thermal sensors, with one side sensitive to THz and the other side emissive in the long wave infrared (LWIR). The sensor heats up upon absorbing incoming THz radiation, and the subsequent rise in temperature can be probed by a commercial LWIR camera. A focal plane array (FPA) of such sensors translates the THz scene to an IR image, captured by the camera. The simplicity of this concept allows the FPA to be used as a simple attachment for IR cameras. The main advantage of this approach is that there is no need for electronics or complex optical readouts, making it very attractive for use in small satellites. The objective of this thesis is to design a MEMS THz-to-IR converter FPA with broadband capabilities. The main requirements are sensitivity between 0.5 and 10 THz and emissivity only on the band of the LWIR camera (7–14 μm). The research is constrained by requirements that allow integration onto a CubeSat (Cubic Compartmentalized Satellite) for concept demonstration in the space environment (specifically low Earth orbit) in future work.

14. SUBJECT TERMS infrared, terahertz, IR, THz, imaging, converter, satellite, CubeSat, cube satellite, cubic satellite, satellite integration	**15. NUMBER OF PAGES** 71
	16. PRICE CODE

17. SECURITY CLASSIFICATION OF REPORT	**18. SECURITY CLASSIFICATION OF THIS PAGE**	**19. SECURITY CLASSIFICATION OF ABSTRACT**	**20. LIMITATION OF ABSTRACT**
Unclassified	Unclassified	Unclassified	UU

NSN 7540-01-280-5500

Standard Form 298 (Rev. 2-89)
Prescribed by ANSI Std. 239-18

THIS PAGE INTENTIONALLY LEFT BLANK

Approved for public release. Distribution is unlimited.

DEVELOPMENT OF A WIDEBAND THZ FOCAL PLANE ARRAY FOR SPACE APPLICATIONS

Anish H. Bhatt
Lieutenant, United States Navy
BSAE, Virginia Tech, 2011
BS, Virginia Tech, 2012

Submitted in partial fulfillment of the
requirements for the degree of

MASTER OF SCIENCE IN APPLIED PHYSICS

from the

NAVAL POSTGRADUATE SCHOOL
June 2020

Approved by: Fabio D. Durante Pereira Alves
Advisor

Wenschel D. Lan
Co-Advisor

Kevin B. Smith
Chair, Department of Physics

THIS PAGE INTENTIONALLY LEFT BLANK

ABSTRACT

This thesis builds upon the research being conducted in the Sensor Research Laboratory in the Physics Department at the Naval Postgraduate School (NPS) in collaboration with the Space Systems Academic Group. The goal is to contribute to the development of MEMS terahertz (THz) to infrared (IR) converters for real-time imaging, with potential applications to the space environment. The NPS MEMS THz-to-IR converters are typically thermal sensors, with one side sensitive to THz and the other side emissive in the long wave infrared (LWIR). The sensor heats up upon absorbing incoming THz radiation, and the subsequent rise in temperature can be probed by a commercial LWIR camera. A focal plane array (FPA) of such sensors translates the THz scene to an IR image, captured by the camera. The simplicity of this concept allows the FPA to be used as a simple attachment for IR cameras. The main advantage of this approach is that there is no need for electronics or complex optical readouts, making it very attractive for use in small satellites. The objective of this thesis is to design a MEMS THz-to-IR converter FPA with broadband capabilities. The main requirements are sensitivity between 0.5 and 10 THz and emissivity only on the band of the LWIR camera (7–14 μm). The research is constrained by requirements that allow integration onto a CubeSat (Cubic Compartmentalized Satellite) for concept demonstration in the space environment (specifically low Earth orbit) in future work.

THIS PAGE INTENTIONALLY LEFT BLANK

TABLE OF CONTENTS

THIS PAGE INTENTIONALLY LEFT BLANK

LIST OF FIGURES

LIST OF TABLES

THIS PAGE INTENTIONALLY LEFT BLANK

LIST OF ACRONYMS AND ABBREVIATIONS

Aluminum	Al
Ar	Argon
BB	Blackbody
c	Speed of Light in a Vacuum = 2.9979 x 10^{8} [m/sec]
CNMS	Center for Nanophase Materials Sciences
COMSOL	COMSOL Multiphysics FE Analysis Software
COTS	Commercial off-the-Shelf
Cr	Chromium
CubeSat	Cubic Compartmentalized Satellite
E&M	Electronic and Magnetic
ε_o	Permittivity of Free Space = 8.85 x 10^{-12} [F/m]
FE	Finite Element(al)
FPA	Focal Plane Array
FTIR	Fourier Transform Infrared Spectrometer
h	Planck's Constant = 6.62 x 10^{-34} [(m^{2*}kg)/sec]
IR	Infrared Electro-Magnetic Range
k	Boltzmann's Constant = 1.38 x 10^{-23} [(m^{2*}kg)/(sec^{2}*K)]
LEO	Low Earth Orbit
LWIR	Long Wave Infrared Range
MEMS	Micro Electro Mechanical System(s)
NPS	Naval Postgraduate School
PECVD	Plasma Enhanced Chemical Vapor Deposition
R	Responsivity
Si	Silicon
SR_{eff}	Selective Radiation Efficiency
SiH_4	Silane
SiN_x	Silicon Nitride–Non Stoichiometric Formulation
SSAG	Space Systems Academic Group
τ_{th}	Thermal Time Constant
ΔT	Change In Temperature
THz	Terahertz Electro-Magnetic Range

THIS PAGE INTENTIONALLY LEFT BLANK

ACKNOWLEDGMENTS

This is my first professional paper, and it has been a difficult learning process. I would like to thank Dr. Fabio Durante Pereira Alves for his guidance, knowledge, patience, and willingness to help with any and all issues I encountered during my simulations research. Without his tireless (almost militaristic) pushing of me to take initiative on my own, I certainly would not be where I am at the end of this thesis period. I would like to thank Dr. Wenschel D. Lan for her input and time in providing information on the operating environment aboard the CubeSat in LEO. Dr. Lan's knowledge and drive in getting funding and logistics worked out for an eventual launch provided me the motivation to push this work forward with pride.

Lastly, I would like to thank my mother, father, and sister. Though they have not specifically helped in my research, it was their phone calls and ability to absorb my discussions that provided me an escape from the daily struggles of an enormous educational workload.

Thank you!

THIS PAGE INTENTIONALLY LEFT BLANK

I. INTRODUCTION

MEMS-based terahertz-to-infrared (THz-to-IR) imaging converters have already been in development using the realm of metamaterials due to a spike in interest in THz imaging [1]. The THz frequency band is synonymous with submillimeter radiation as it lies between the microwave and IR ranges in the E&M spectrum. Due to its non-ionizing nature, incident THz radiation will not affect an object on its atomic level, even after repeated applications. Non-polar and non-metallic objects are subject to some level of penetration by this radiation as well [2]. While THz is not ideal for long distance imaging within Earth's atmosphere due to absorption, it is capable of travelling far off reflected surfaces in the space environment. In fact, this absorption of submillimeter wavelengths is one of the main reasons many submillimeter telescopes are located at high altitudes, to minimize travelled atmospheric distance. In the space environment, relatively colder objects cannot be seen in the infrared (IR) range but can be detected by a THz sensor. Terahertz photon energy peaks at temperatures below 50K, making the vast coldness of space an ideal environment for utilization of such detection bands. Furthermore, object identification may be possible by penetration of the initial cover layers of these objects and reflection off the metallic objects underneath. This reflection can possibly provide characterization of the materials and what purpose they may serve.

Other research groups [3] and industry [4] have been working to develop a sensitive real-time THz imager. Several approaches were demonstrated using different technologies such as infrared microbolometers [5], metamaterial enhanced microbolometers [6], plasma enhanced microbolometers [7], metamaterial based bi-material sensors [8] and THz-to-IR band converters [1]. While all the approaches have their advantages and drawbacks, the latter presents the most simplicity.

A major industrial player worth mention is the TeraSense^{TM} company [4], whose imaging sensors use a broadband surface antenna to receive polarized THz signals. Their patented imaging technology converts incident THz radiation into the alternating potential of a relativistic plasma wave. This plasma wave is in turn proportional to the photo-response signal. The alternating potential rectification process is possible due to

the asymmetry of the plasmonic waveguide, thusly a specific THz band can be tailored by varying their detector geometry. The TeraSense manufacturing process is similar to the method followed at the Naval Postgraduate School (NPS), utilizing class 1,000 and class 100 cleanrooms. However, the TeraSense process uses GaAs (Gallium Arsenide) wafers, as opposed to the Si wafer substrate used at NPS. In both methods, the fabrication process involves photo-resist spinner application, UV exposure and electron beam lithography for photo-resist removal, metal deposition, photo-resist asher, and finally an ion etching system. Figure 1 is provided by the company as a visualization of their basic concept of operation.

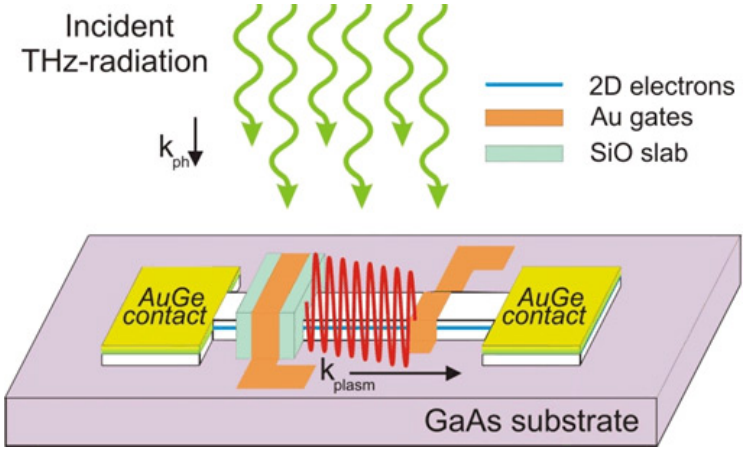

Figure 1. TeraSense Submillimeter Imaging Concept. Source: [4].

While the plasma-enhanced micro-antenna detector from TeraSense has become a commercial product, it is complex to fabricate and requires dedicated on-chip microelectronics readouts. An attractive way to simplify the readout is to convert the THz energy in every pixel of an array to another band (i.e., visible and infrared) that can be imaged by commercially available cameras.

One attractive approach for THz imaging is through band conversion. Reference [1] describes the work done in this field since the 1950s. More recently, a concept for converting THz energy into the visible light band is being researched by a team at Durham University, United Kingdom, led by Kevin Weatherill [3]. Weatherill's team

aims to improve the frame rate of THz capture, a task proven difficult so far in the industry due to decreased sensitivity sensors and power of sources. Their technique vaporizes Cesium atoms in a quartz cell and exposes them to IR lasers operating at specific frequencies. The associated electrons are excited to their Rydberg states before decaying to their ground states. The teams are finding that the Rydberg state Cesium atoms are "very sensitive to the incident terahertz field" [3]. Once the Cesium atoms are excited to their IR associated Rydberg state, further submillimeter radiation is then shined on them (after passing through the object to be imaged). The THz photon excited Rydberg state Cesium electrons have been found to have a 52.4% chance of emitting a 535 nm (green) photon upon random decay back to their ground states. All the combined green photons emitted due to the THz radiation can image a "shadow" of the original object being viewed in THz. These green photons can then be picked up by a standard (or green optimized) commercial off-the-shelf (COTS) camera with a high frame rate for high quality video imaging, providing another indirect THz imaging technique. Figure 2 shows the concept of excited states of the Cesium atoms and emission of the green photons.

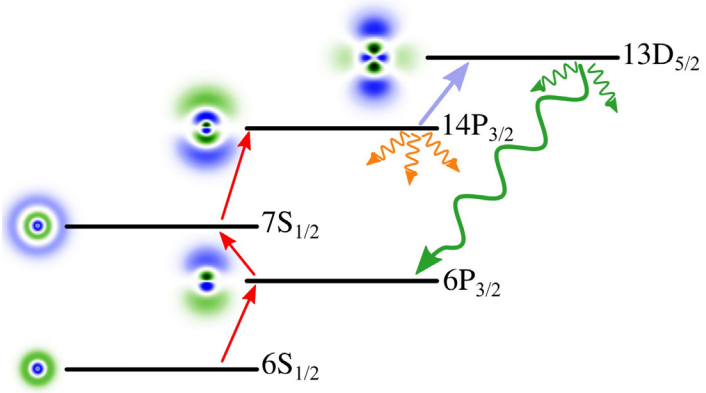

Figure 2. Excited Cesium Decay Photon Emission Concept. Source: [3].

The THz to visible wavelength approach is interesting and allows for a very high speed of operation. However, this method is still complex and requires a well-tuned laser for excitation in order to work.

A much simpler and completely passive approach was proposed by our group; the technique was based on conversion from narrowband THz to long-wave infrared (LWIR) [1]. The MEMS converters were based on double metamaterial films to achieve THz absorption on the front side of the detector and IR emission on the backside, which was read by a COTS LWIR camera. While a good band conversion efficiency of approximately 5% had been achieved, the metamaterial structures comprised three layers of metal and two layers of dielectric, making the thermal mass relatively high. The increased thermal mass made the sensor relatively slow with a thermal time constant (τ_{th}) of about 150 ms.

To adapt the sensor for space applications, we attempted to further simplify microfabrication—make the detection of THz broader, and reduce thermal mass to increase the speed of operation. The NPS Physics Department Sensors Lab is investigating a new approach based on nanoscale metallic films deposited onto dielectric thin films. Figure 3 shows the concept of operation.

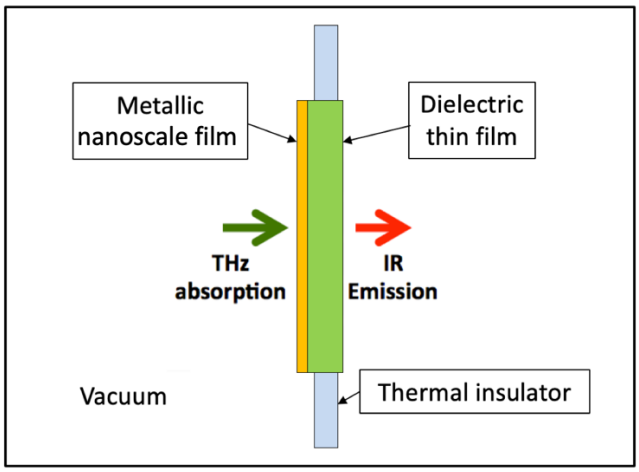

Figure 3. THz-to-IR Conversion Concept (Individual Pixel)

The metallic nanoscale film absorbs incident THz radiation and further heats up the sensor structure. To reduce heat conduction, the sensor is thermally isolated and placed in a vacuum to mitigate thermal loss due to convection. The IR emitting backside temperature is modulated by the absorbed THz power. This temperature difference is

translated to radiance changes in the LWIR band, which can be probed by a LWIR camera. The THz-to-IR focal plane array (FPA) is a matrix of each of these individual pixel sensors and can further be integrated onto a COTS LWIR camera for space operation, as shown conceptually in Figure 4. The full imager assembly consists of THz focalization and filter optics, vacuum chamber containing the FPA, IR focalization optics, and finally, the LWIR camera. In Figure 4 the dark firmament (in the visible and IR) is being imaged by our assembly, while the resulting cold objects are revealed on the IR camera display.

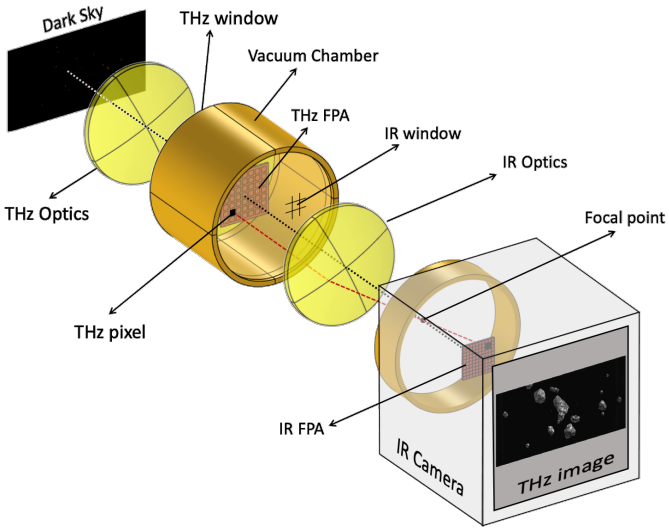

Figure 4. THz-to-IR Imager Concept

Once the THz imager is ready, it will be integrated onto a small satellite, in a 6U CubeSat form factor, by the NPS Space Systems Academic Group (SSAG) and perform a series of tests in low earth orbit (LEO). Due to the vacuum of space, the vacuum chamber will not be necessary.

In this context, the objective of this thesis is to design a broadband THz-to-IR converter FPA using nanoscale metal films with dielectric thin film structures for potential space applications. To achieve this objective, our research work has been

conducted as described in this thesis, organized in Chapters, as summarized in the following paragraphs.

Chapter II describes the theory and calculation methodology behind thermal sensors and band conversion. Our calculation methodology made large use of the FE analysis simulations available in COMSOL Multiphysics. Material properties, sensor morphology, boundary conditions, and numerical approximations are then considered within COMSOL to build a design method for individual pixels. The envisioned sensor and material and geometric configuration selection is then described in detail. Figures of merit of the sensor are calculated using a team-built FE model. Lastly, the basic aspects of sensor radiation efficiency are discussed.

Chapter III contains the analysis of the impact of the materials, geometry and environmental conditions upon the sensor responsivity, thermal time constant and efficiency. Both figures of merit are analyzed for variations of emissivity and absorptivity of the sensor surfaces of the developed FE analysis model; an optimum configuration is then suggested.

Chapter IV contains the important aspects of fabrication and characterization of the Cr and SiN_x films. Details of NPS' microfabrication capabilities and MEMS techniques are discussed. The characterization process is detailed while experimental results are compared with simulated expected characteristics. The fabrication procedures for the complete focal plane array are also suggested.

A brief conclusion is provided in Chapter V, where the most important findings are highlighted and a final design to be fabricated in future work is provided. In addition, some suggestions on how the modeling and analysis can be improved are listed.

II. THEORY AND MODELING ASPECTS

A thermal sensor can be described as a sensing element connected to a much larger thermal mass that acts as a heat sink; normally the substrate or structural hardware; through thermally insulating anchors or beams. Upon absorption of incident radiation, ΔP, the temperature of the sensing element increases by an amount ΔT. ΔT depends on the level of thermal insulation of the sensing element, among other factors. The three fundamental heat loss mechanisms, conduction, convection and radiation are represented by a single term, thermal conductance (G_{th}). Figure 5 shows a diagrammatic representation of a typical thermal sensor.

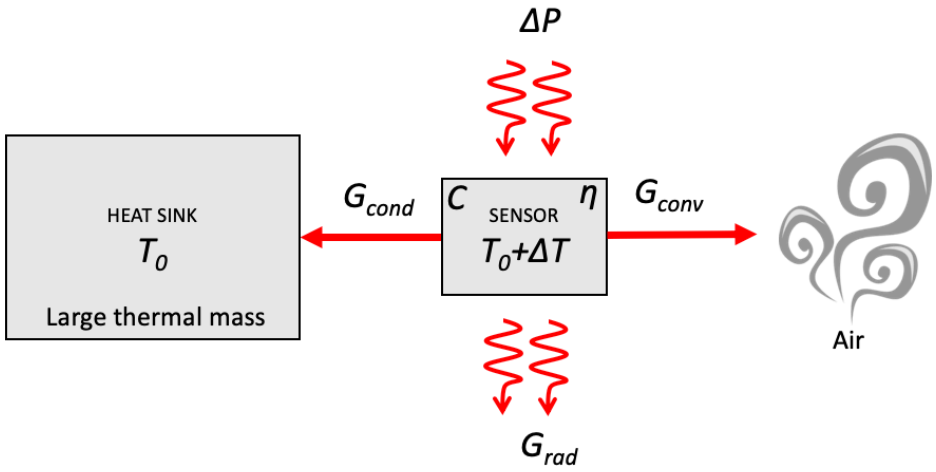

Figure 5. Schematic Diagram of Typical Thermal Sensor Operation

The heat balance equation for this system is given by Equation (1).

$$C_{th}\frac{d(\Delta T)}{dt}+G_{th}\Delta T=\eta\Delta P \qquad (1)$$

Here, η is the absorptivity of the sensing element (fraction of the absorbed power per incident power on the sensor). C_{th} is the thermal capacitance of the sensor measured in $[\frac{J}{K}]$ and is given by Equation (2).

$$C_{th} = c_{th}\rho A_s t \qquad (2)$$

Here, c_{th} is the material's thermal capacity, ρ is the material's density, A_s is the surface area, and t is the structure's thickness. The thermal capacitance of the sensor is the sum of thermal capacitances of all material layers. Most thermal detectors are made to operate in vacuum, therefore convection can be considered negligible and thermal conductance can be represented by the summation of the remaining two heat loss terms, concoction (G_{cond}) and radiation (G_{rad}). Conduction is given in Equation (3).

$$G_{cond} = \frac{g_{th} A_c}{l} \qquad (3)$$

Here, g_{th} is the thermal conductivity, A_C is the cross-sectional area and l is the length of the thermal insulating beam. Heat loss through radiation is defined in Equation (4).

$$G_{rad} = \frac{d}{dT}\left[\pi A_s \int_0^{\infty} \eta_i(f) L_{0f}\, df\right] \qquad (4)$$

Here, A_s is the surface area of the sensing element and η_i is the frequency dependent emissivity/absorptivity of the surface (i=1 and 2 assuming the sensing element has two sides). The spectral radiance is L_{0f}, measured in $[\frac{W}{m^2 * sr}]$ and is given by Equation (5).

$$L_{0f} = \left(\frac{2hf^3}{c^2}\right)\frac{1}{e^{hv/kT} - 1} \qquad (5)$$

Here, T is the absolute temperature of the sensing element which is the starting ambient temperature plus the change; $T = T_0 + \Delta T$. In most practical detectors ΔT is small, therefore all intrinsic material properties can be considered constant at T_0. The solution of Equation (1) when the incident power is periodic and possesses angular frequency ω, is given by Equation (6).

$$\Delta T = \frac{\eta \Delta P}{G_{th}\sqrt{1 + (\omega \tau_{th})^2}}, \qquad (6)$$

Here $\tau_{th} = C_{th}/G_{th}$ is the thermal time constant of the sensor. For a slow varying ΔP ($\omega << 1/\tau_{th}$) the temperature difference in the sensor can be approximated by Equation (7).

$$\Delta T = \frac{\eta \Delta P}{G_{th}}. \qquad (7)$$

The main figures of merit analyzed in this work are thermal time constant and responsivity, R [k/W], given by the ratio of temperature change to incident power change ($R = \Delta T/\Delta P = \eta/G_{th}$). For faster detection τ_{th} must be small. There are two ways to reduce τ_{th}; firstly, by reducing the thermal capacitance (thermal mass) by making the sensing element as thin as possible; secondly, by increasing G_{th}. Notice that increasing thermal conductivity reduces R, therefore this property must be engineered according to the application demands where a compromise between both figures of merit must be found.

In our particular case of a thermal sensor band converter, one side of the sensing element absorbs the band of interest (THz) and the other side emits in a different band (LWIR) to be probed by another sensing system. As detailed in [1], band conversion is not a new idea and has been researched by several groups since the early 1950s. With the advancement of MEMS technology this idea has become more obtainable.

The focus of this research effort is on a MEMS based THz-to-IR band converter FPA to be used in space imaging applications (as depicted in Figure 4). Our FPA utilizes nanoscale metal films as a broadband THz absorber [6]. A thin dielectric layer acts as a selective IR emitter [9] (see Figure 3) as well as a structural layer. Our resulting MEMS sensor was conceived as shown in Figure 6.

The top left part of Figure 6 shows a partial array of pixels while the top right shows the top view of a single pixel. There, the free-standing sensing element (1) is connected to the substrate (3) by four symmetrically located thermal insulator beams (2). The top side, highlighted on the bottom left is comprised of an ultra-thin metallic film that exhibits broadband THz absorption properties. The bottom side of the sensor, shown on the bottom right of the figure is comprised of a dielectric layer that serves three purposes. The first purpose is to act as a selective emitter in the LWIR to provide functionality to the band converter. The second purpose of the dielectric layer is to serve as a structural layer of the MEMS free-standing sensing element. The third and final

purpose of the dielectric layer is to serve as a thermal insulator, providing functionality to the thermal sensor. Using the same material utilization for IR emission and thermal insulation materials tremendously simplifies the fabrication of such a device. The vertical dimensions in the figure are out of proportion for ease of visualization.

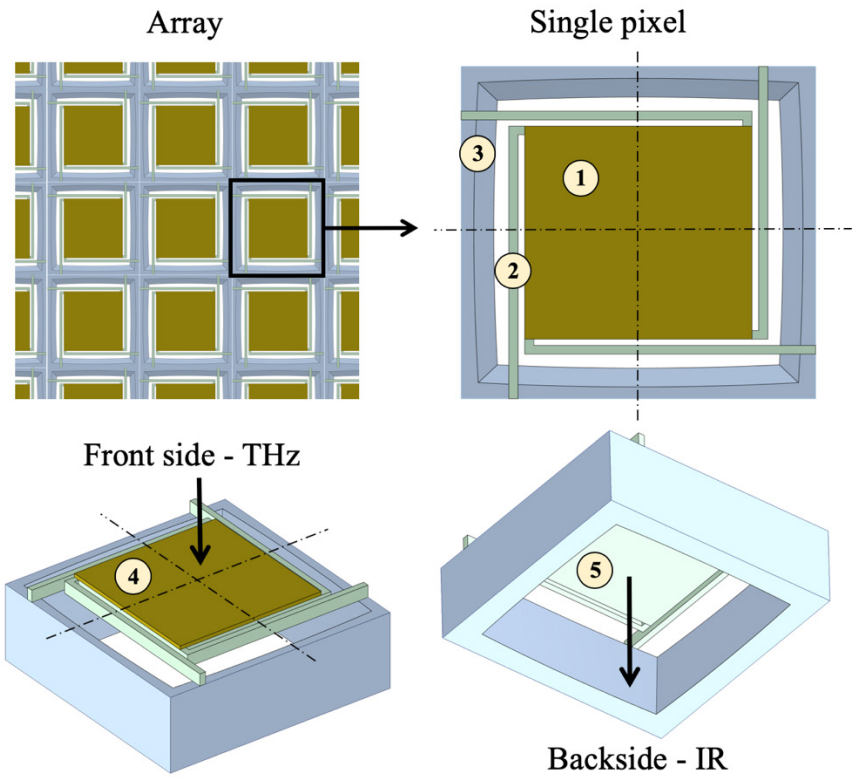

Numerical Representation: (1) Sensing Element; (2) Thermal Insulating Beam; (3) Substrate; (4) Nanoscale Metal Film (THz Absorber); (5) Dielectric Pixel Structure (IR Emitter). Vertical dimension out of proportion for visualization ease.

Figure 6. Schematic Diagram of MEMS THz-to-IR Band Converter FPA

Another important characteristic is the symmetry, highlighted by the symmetry axes in Figure 6. Using this property, the functional part of the pixel can be divided into identical four quadrants. By conducting analysis using only one quadrant, the computational efforts can be significantly reduced. Figure 7 shows the details of one quarter of a pixel supported on the substrate frame. The parameters shown in the figure are sensing element size (d_s), thermal insulator beam length (l_l), thermal insulator beam

width (l_w), metal thin film thickness (t_{metal}), dielectric thickness (t_{diel}) and substrate thickness (t_{subs}). As in Figure 6, the vertical dimension in Figure 7 are out of proportion for visual purposes.

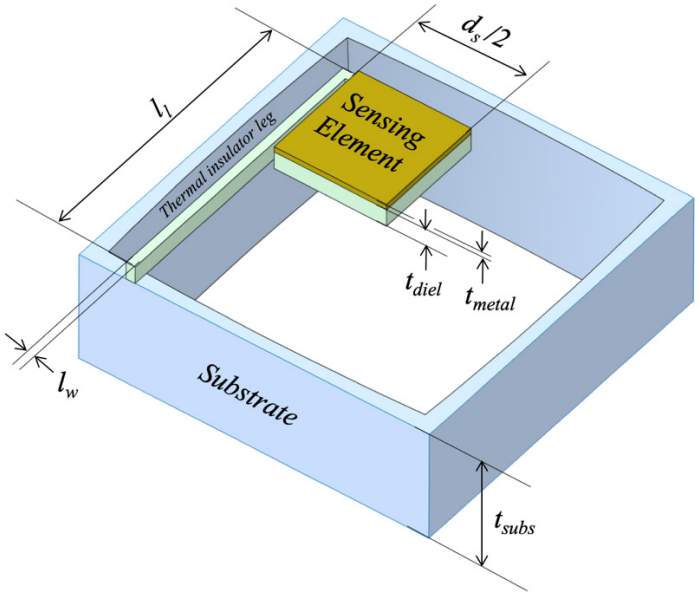

One quadrant of a single pixel sensing element is shown. Dimensional parameters: Sensing Element size (d_s); Thermal Insulator Beam length (l_l); Thermal Insulator Beam width (l_w); Metal Thin Film thickness (t_{metal}); Dielectric thickness (t_{diel}); Substrate thickness (t_{subs}). Vertical dimension out of proportion for visualization ease.

Figure 7. Schematic Diagram of MEMS THz-to-IR Band Converter Pixel

In order to design a sensor to exhibit the desired figures of merit, R and τ_{th}, it is necessary to select appropriate materials and dimensions. The materials were selected based on NPS's microfabrication facility capability and legacy knowledge base from previous projects. Several metals can be deposited within NPS's cleanroom; however, the preferable ones are those with low conductivity such as chromium (Cr) and nickel (Ni).

According to Alves et al., the maximum absorptivity occurs when the condition laid out in Equation (8) is met [6].

$$\sigma t_{metal} = 2c\varepsilon_0. \qquad (8)$$

Here σ is the electrical conductivity of the metal and t_{metal} is the thickness of the film. The numerical value of the right hand side of Equation (8) is approximately 0.0053; therefore, to keep the film thickness on the order of tenths of nanometers the conductivity of the metal must be between 10^5 to 10^6 [S/m] where the unit "S" is Siemens. Thusly, Cr and Ni are two potentially appropriate candidates with the conductivity of Ni being greater than that of Cr. In order to maximize THz absorptivity; the films of Ni and Cr must be very thin at ~2 nm and ~10 nm, respectively. Figure 8 shows the THz absorptivity and film conductivity of both materials over varying film thickness.

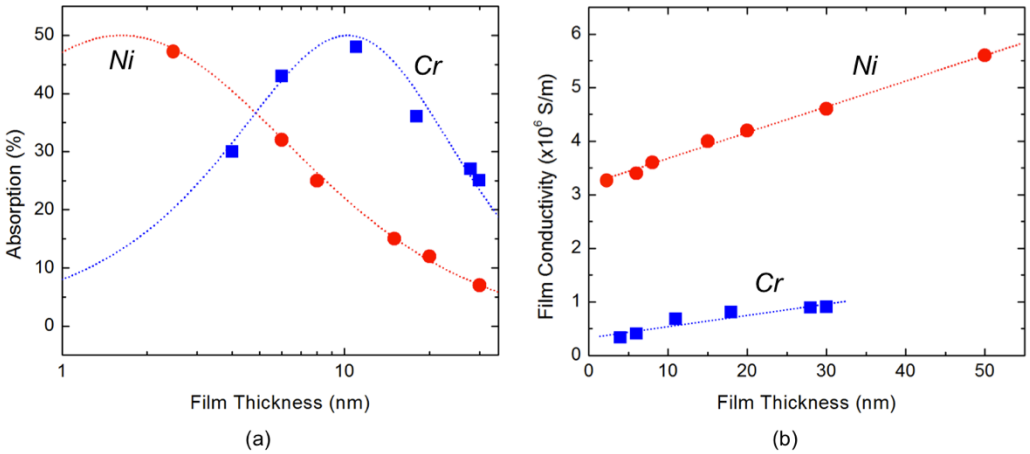

(a) Experimental (circular markers for Ni and square markers for Cr) and calculated (dotted lines) absorption of Cr and Ni samples as a function of film thickness. (b) Relationship between conductivity and film thickness for both metals, dotted lines are linear fits.

Figure 8. THz Absorptivity and Conductivity over Film Thickness. Source: [6].

Chromium was selected as the metal of choice because it requires greater thickness than Nickel. Depositing 10 nm Cr is much easier than 2 nm of Ni. A precise control of the thickness below 5 nm is difficult with the available deposition instrument. It can be observed in Figure 8 that the maximum broadband THz absorptivity of a metallic thin film is 50% [6], therefore this is the maximum absorptivity that can be achieved by the sensor.

For the dielectric layer, both Si rich silicon oxide (non-stoichiometric SiO_x, $x < 2$) and SiN_x were considered. Both dielectric materials are MEMS fabrication friendly and exhibit low residual stress in free standing membrane form [10]. Due to the actual configuration of the Plasma Enhanced Chemical Vapor Deposition (PECVD) machine at NPS, SiN_x films are easier to be obtained. The selectivity of SiN_x films on the LWIR range is an object of study and will be presented in the subsequent chapter. The impact of the SiN_x layer on THz absorption is negligible for three reasons; most of the THz absorption happens on the metal layer, the extinction coefficient of SiN_x in the THz range is very small, and the SiN_x is very thin. According to Kirchhoff's law, emissivity and absorptivity are the same [11]. Throughout this thesis, the term absorptivity will be used for the Cr layer (sensing film) and emissivity will be used for the SiN_x layer (emitting layer). It was reported in a previous publication [12] that measurements of absorptivity are much simpler to perform using spectrometry and are able to provide an accurate estimate of emissivity. Finally, the substrate of choice is Si due to the availability of processes to deposit films onto it, etch structures on it, and deep Si etch (Bosh etch) it. The Bosch etch serves to remove the substrate from the backside of the sensor, exposing the nitrate layer.

The pixel dimensions were selected based on legacy knowledge from our research group on THz sensors. This knowledge was gleaned from studies considering diffraction limit, amount of THz power captured at the sensing element area and fabrication constraints. Based on information compiled from [1], [8] and [13], an adequate size for a THz sensing element is about $200x200\mu m^2$. Consequently, a pixel size of about $360x360\mu m^2$ allows for enough room for both the thermal insulating beams and the backside opening while providing a solid frame for the sensing element to hang.

The concept of operation of the THz-to-IR converter relies on broadband absorptivity of the Cr thin film in the THz range and selective emissivity in the LWIR range of the SiN_x film. Intuitively, it can be inferred that the highest conversion efficiency is achieved when the absorptivity of the Cr film is the highest possible in the THz band of interest and near zero elsewhere while the emissivity of the SiN_x film is

near unity in the IR band of the infrared used as a readout and near zero elsewhere. Figure 9 illustrates the concept.

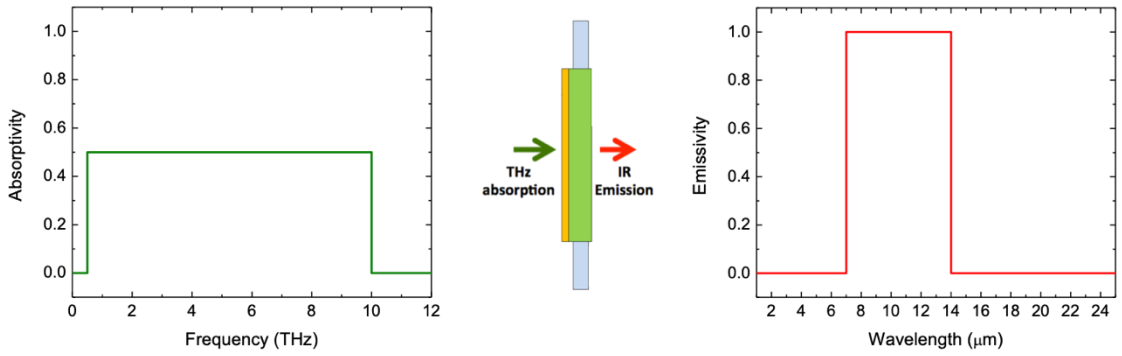

(Left): Ideal (desired) THz absorptivity of Cr film; (Right) Ideal (desired) IR emissivity of dielectric thin film to maximize conversion efficiency.

Figure 9. Ideal Situation Representation of THz Absorption and IR Emission

In order to measure the selective radiation efficiency SR_{eff} of the sensor we define a new figure of merit. This figure of merit is the ratio between the backside radiated power (within the readout of the IR camera band) to the total radiated power by the sensor (from both sides). This number can provide a sense on how selective the absorbing and emitting films are in the bands of interest and what is the fundamental limit (maximum) efficiency that can be achieved. Assuming both sides of the sensing element can be approximated as Lambertian radiators [14], SR_{eff} can be expressed mathematically by Equation (9).

$$SR_{eff} = \frac{A_s \pi \int_{f_1}^{f_2} \left(\varepsilon_{IR}(f) \left[L_{0f}(T_0 + \Delta T) - L_{0f}(T_0) \right] \right) df}{A_s \pi \int_{0}^{\infty} \left(\left(\varepsilon_{IR}(f) + \eta_{THz}(f) \right) \left[L_{0f}(T_0 + \Delta T) - L_{0f}(T_0) \right] \right) df} \qquad (9)$$

For the numerator of Equation (9) A_S is the surface area of the sensing element, the multiplicative π outside the integral is the hemispherical projected solid angle [sr], ε_{IR} is the emissivity of the backside of the sensor, and the integration limits are the frequency limits imposed by the COTS IR camera spectral response (IR camera limits). For the

denominator of Equation (9), η_{THz} is the absorptivity of the front side of the sensing element and the integral is performed over the full E&M spectrum. The surface area from the backside and front side are the same (illustrated in Figure 6), therefore the terms $A_S\pi$ will cancel.

Next, a study on the impact of the material properties and dimensions of the pixel on the sensor figures of merit must be conducted. Due to the complexity presented by a full physical model of the sensor, FE simulations of our quartered model (Figure 7) was the preferable method of analysis. The FE simulations were performed using COMSOL Multiphysics (COMSOL^{TM}).

The quartered pixel geometry was simulated using the solid mechanics and heat transfer modules built into COMSOL. In order to allow thermal and structural properties to be correctly calculated, symmetry boundary conditions were applied to the surfaces on the cutting planes. All parts were considered linear elastic materials and were structurally unconstrained except for the substrate frame, which was supported on the edges. To further reduce computational efforts, the surface of the thermal insulating beam touching the Si frame was set as a mechanically fixed constraint and the substrate was removed from the simulation. In addition to these model considerations, the same surface was set to a fixed temperature depending on ambient conditions in both the laboratory and the space environment to account for the heat sink effect of the substrate. The ambient temperature was varied for three values (-40, 20, 80^{o} C) based on the approximate operating envelope of the 6U spacecraft estimated by the potential CubeSat bus vendor [15]. The front surface of the sensing element was set as an inward heat flux, representing the THz incident power absorbed by the metallic Cr film. The heat flux was calculated as 1 μW divided by the surface area of the sensing element, A_S (1μW/A_S), therefore, all temperature differences computed would be normalized per μW. The final structure was meshed using free triangles on the backside surface of the structure, and extruded through the vertical dimensions to all material domains. Because the aspect ratio of the geometry between the horizontal and vertical dimensions is very high (> 200), only one mesh element per domain in the vertical direction. This can be done because the expected

temperature gradient between the edges of the domains is very small. On the horizontal dimension a reasonable, fine mesh was used (> 50 elements per surface).

Time dependent simulations were also performed to determine both the R and τ_{th} of the sensor. Initially, absorptivity and emissivity of both layers were kept constant over the spectrum.

Figure 10 shows two views of the quartered pixel COMSOL geometry. On the left side, the vertical dimension (Z axis) is exaggerated by a factor of 200 to allow identification and manipulation of the layers with different materials. On the right side, the to-scale view is shown to highlight the actual aspect ratio. All temperature readings, were taken on the interface between the Cr and Ni layers. Specifically at the interface, the point measured is indicated in the figure, labeled as "Point 17".

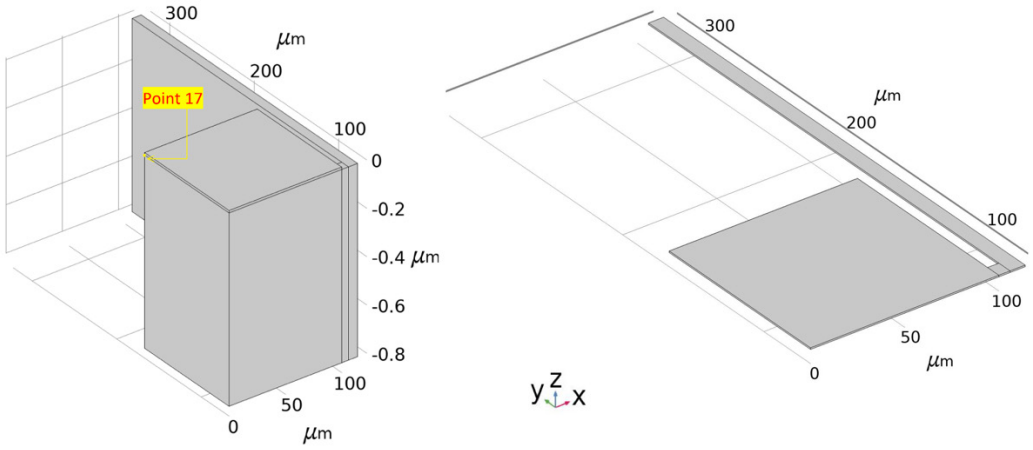

(Left): Z axis exaggerated with Point 17 at interface highlighted; (Right): True scale representation.

Figure 10. Single Pixel COMSOL Geometry (Quartered)

In order to estimate both R and τ_{th} in a single run, the inward heat flux representing the THz incident power was pulsed at a repetition rate referred to as the gate frequency. A single "pulse cycle" involves turning the THz source on and off. In order to emulate a constant incident power and capture the steady state (equilibrium) temperature difference, we simulated a relatively low gate frequency starting at 1 Hz. The emissivities

for the Cr and SiN_x outer surfaces were set to 0.5 and 0.9, respectively. The heat flux was set to $25W/m^2$, which equates to 1μW incident on the entire surface of the sensing element. The resulting time dependent temperature profile of a single pixel is shown in Figure 11, the initial temperature (room temperature) is 293.15 K and the final temperature (at 0.5 seconds) is 293.57 K.

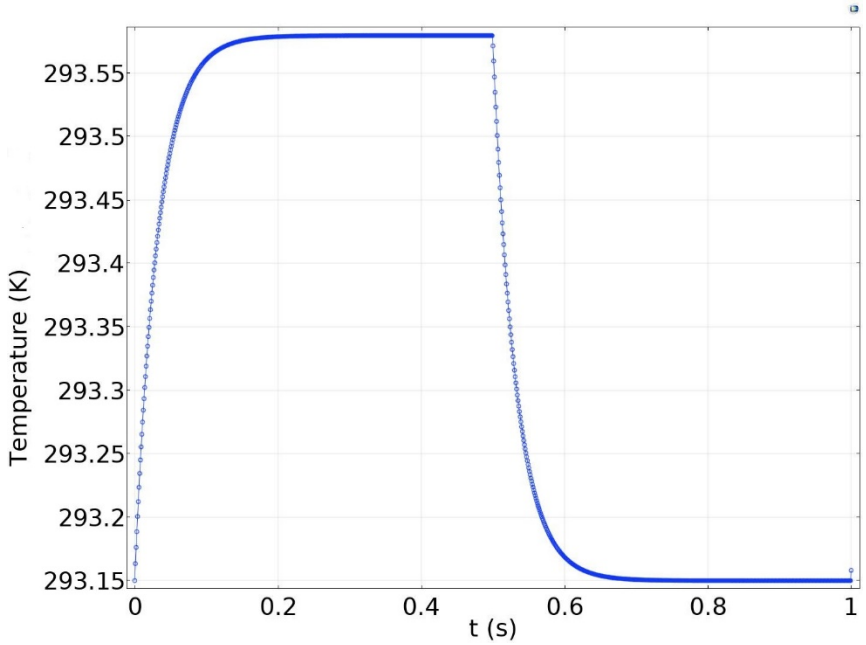

Figure 11. Temperature Variation of Pixel over Time – 1 Hz Gate Frequency

From the data plotted in Figure 11 it is possible to estimate responsivity as (293.57-293.15)[K]/1[μW] = 0.42 K/μW. In addition, the thermal time constant can be estimated by fitting the sensor thermal response over time to an exponential function. This procedure was performed in Matlab™, and the fitting function is given by Equation (10).

$$T(t) = 293.67 - 0.42\exp(-31.23t) \qquad (10)$$

The corresponding equation with the simulated quantities is given by Equation (11).

$$T(t) = T_{final} - \left(T_{final} - T_{initial}\right)\exp(-\frac{t}{\tau_{th}}) \qquad (11)$$

For this particular simulation at room temperature, the thermal time constant is 32 ms (compare Equations (10) and (11)).

The frequency response of the sensor was also analyzed by repeating the simulation as the gate frequency is increased. As gate frequency increases the sensor has less time to react, and at a certain frequency a temperature difference rollover will start. Figure 12 shows the time response for several sample gate frequencies. According to the data output of Figure 12, the temperature maximum is approximately 293.56K for 5Hz, 293.47K for 15Hz, 293.43K for 25Hz, and 293.39K for 80Hz.

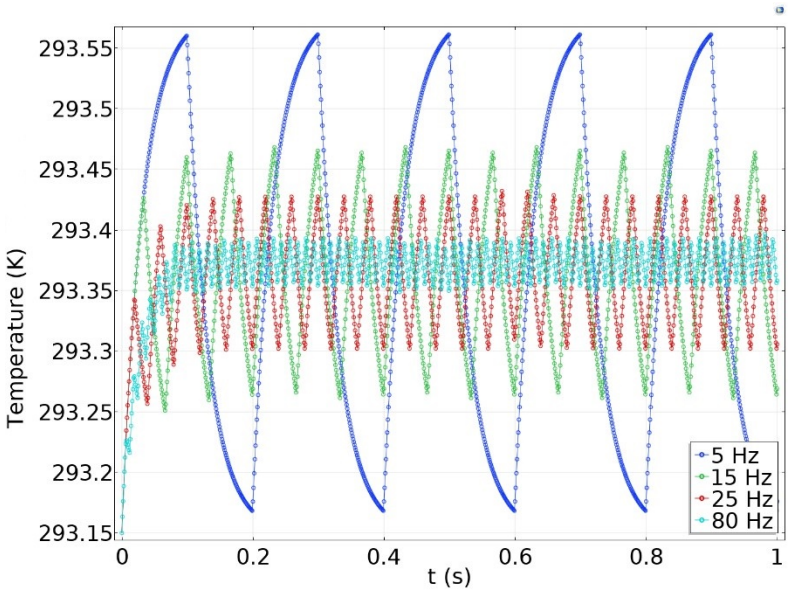

Figure 12. Temperature Variation of Pixel over Time – Increasing Gate Frequencies

Figure 13 shows the frequency response of the sensor obtained by running a parametric simulation of the gate frequency between 1 and 100 Hz. The temperature difference (peak to peak ripple) was normalized by ΔT at a gate frequency of 1 Hz. The cutoff frequency (f_0) is computed when power reaches one half of the initial value, or

when the normalized ΔT magnitude reaches $\frac{1}{\sqrt{2}}$. This cutoff frequency defines the operational speed of the sensor. The τ_{th} value can also be computed by Equation (12).

$$\tau_{th} = \frac{1}{2\pi f_0} \qquad (12)$$

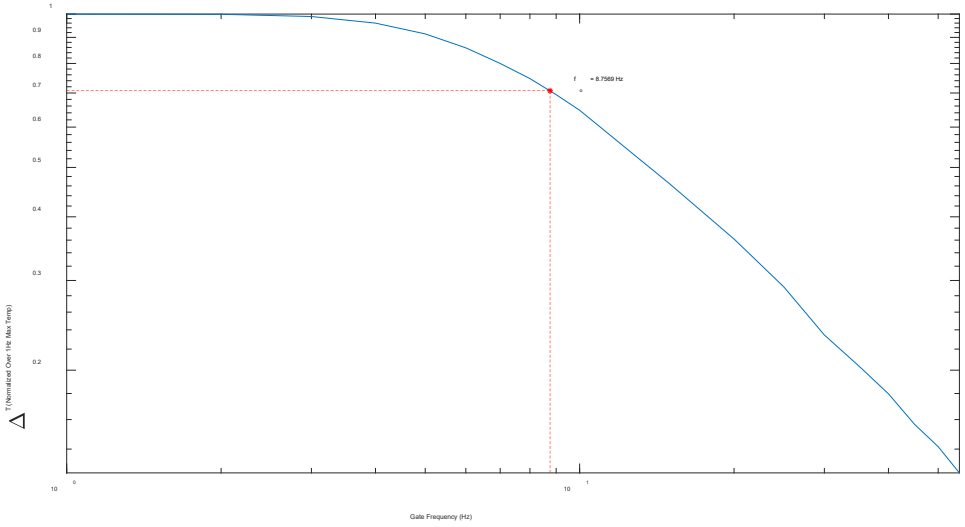

Figure 13. Frequency Response of THz-to-IR Band Converter

From Figure 13, we see that f_0 = 8.76Hz, which makes τ_{th} = 18.2 ms. Note that the frequency response method estimates a smaller thermal time constant than the time domain exponential fitting method. The discrepancies are most likely coming from the frequency response calculation. The exponential fitting was the method of choice because it gives a more conservative (longer) τ_{th}, introduces less error, and requires much less computational effort to calculate.

THIS PAGE INTENTIONALLY LEFT BLANK

III. ANALYSIS

FE analysis simulation was extensively utilized with the models described in the previous chapter to understand the impact of the material properties (absorptivity & emissivity) of the front and backside layers of the THz-to-IR pixel sensing element. These properties can be manipulated by alterations to fabrication conditions and techniques to place the sensor characteristics closer to the desired properties. Several scenarios were examined with varying conditions and property variations. A collection of results extracted directly from COMSOL and post-processed in Matlab is available in the appendix. The key results are summarized in the following paragraph.

Initially, the ideal case was simulated. Recall that the ideal case is illustrated in Figure 9 where the absorptivity of Cr is 0.5 between 0.5 and 10 THz and zero elsewhere, and the emissivity of SiN_x is 1 between 7 and 14μm and zero elsewhere. The ambient temperature was initially set to 20 ° C (293.15 K) and subsequently changed to -40 ° C (233.15 K) and 80 ° C (353.15 K), which represent the estimated operating temperature extremes of LEO where the sensor will be employed. Figure 14 shows the resultant temperature gradient on the sensor when the incident power on the Cr side is kept constant at 1 μW at 20° C ambient. The resulting temperature difference between extremes is measured from the center of the sensing element to the substrate frame.

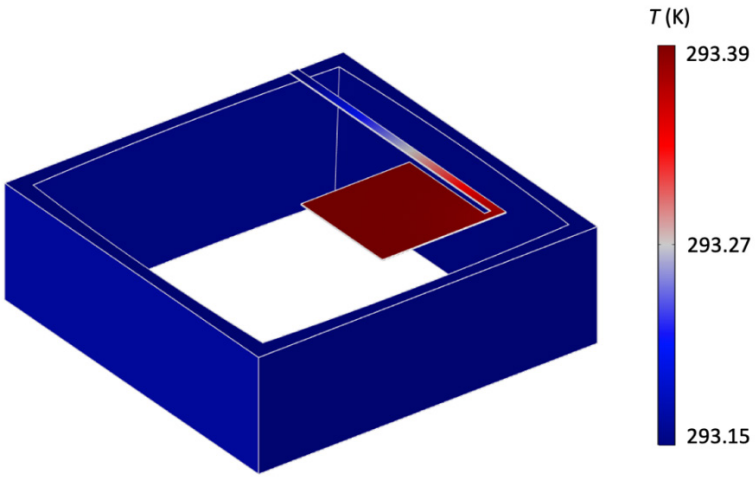

Ideal absorptivity/emissivity properties are modeled at 20°C ambient temperature with constant 1 μW power applied.

Figure 14. Surface Temperature Plot of Quartered Pixel with Substrate

Next, the Cr absorptivity was varied from 0.1 to 0.5 (maximum) while SiN_x emissivity was kept at the ideal value of 1. Figure 15 shows the responsivity of the sensor operated at the aforementioned ambient temperatures.

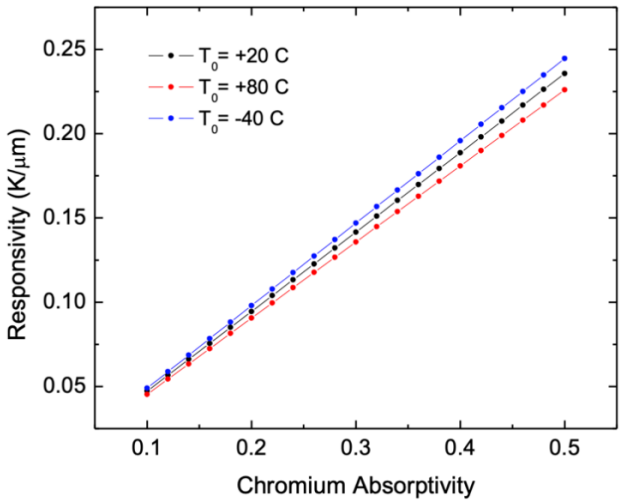

Responsivity of the THz-to-IR sensor for ideal selectivity properties of both layers (see Figure 9). Three ambient temperatures are simulated for the LEO operating envelope.

Figure 15. Responsivity over Cr Absorptivity – Ambient Temperature, Simulated

It is clear from Figure 15 that the greater the Cr absorptivity, the greater the responsivity. This result is expected as more of the incoming power is converted to heat. Due to an increase in its absorptivity (emissivity), the Cr film irradiance does not compete significantly with heat absorption. Therefore, it is best to have this layer at its maximum absorptivity. Observe that the responsivity is greater for lower ambient temperatures—exposure to extreme ambient operating temperature swings will occur in LEO, so the responsivity will have to be calibrated for the full temperature range, since the sensor element shows temperature dependency.

The 20ºC scenario was initially selected and the responsivity was calculated for other cases in addition to the ideal absorptivity and emissivity; Figure 16 shows the results. The black markers and line represent the ideal case, extracted from Figure 15. The blue markers and line represent a case where the SiN_x layer approaches blackbody (BB) behavior, therefore emissivity is unity over the entire spectrum. All the other colors represent a case where the SiNx layer only emits at LWIR (7-14μm) and the emissivity varies from 0.5 (red) to 0.9 (dark cyan). Figure 16(b) shows a zoomed in view of the higher values of Cr absorptivity to highlight the effects of the SiN_x emissivity.

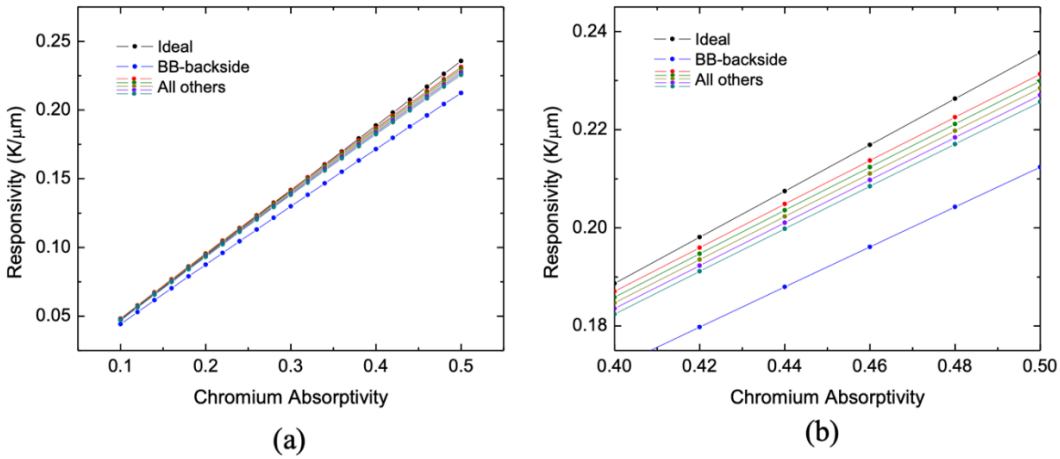

(a) Responsivity of THz-to-IR sensor at ambient temperature of 20ºC over Cr absorptivity, SiN_x emissivity varied from 0.5 to 0.9 under "All others." (b) Magnification of (a) for higher fidelity

Figure 16. Responsivity over Cr Absorptivity – SiN_x Emissivity, Simulated

It is clear from Figure 16 that the ideal case exhibits the greatest responsivity while the BB case exhibits the worse responsivity. This responsivity result is expected in the BB case since the sensor is radiating at its maximum over the entire electromagnetic spectrum. This radiation over the entire spectrum causes more heat loss than in any other case. Both ideal and BB cases represent the fundamental limits of responsivity. Any selectivity and/or emissivity that can be manipulated by fabrication techniques on the SiN_x layer will always be within the ideal and BB limits. Note that as SiNx emissivity increases the responsivity slightly decreases and the range is not great—less than 10mK/μW for the highest value of Cr absorptivity.

The thermal time constant was also analyzed for all the aforementioned scenarios. Figure 17 shows the first 200 ms of the transient response of the sensor to a pulsed stimulus for all three ambient temperatures considered in this analysis. This time interval was found to be enough to estimate τ_{th} using the exponential fitting method discussed in Chapter II.

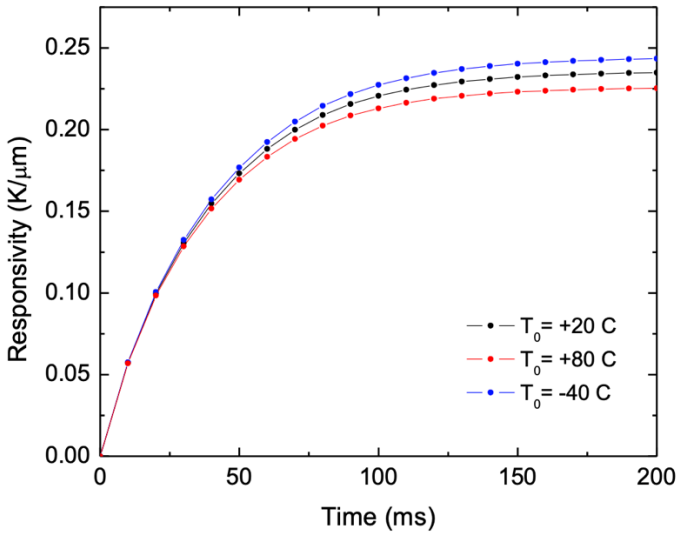

Figure 17. Transient response of THz-to-IR sensor for ideal case of both layers (see Figure 9 for ideal case visualization) for three ambient operating temperatures.

Figure 17. Transient Response – Ideal Case of Both Layers

The behavior shown in Figure 17 is in agreement with the responsivity results shown in Figure 15. Keeping the SiN_x emissivity constant at 0.9 at the desired band (which we believe is achievable experimentally), the transient response of the sensor for Cr absorptivity varying from 0.1 to 0.5 was simulated and the result is shown in Figure 18(a). As expected, the final responsivities increase with the absorptivity; however, the steady state is achieved at almost the same time into the transient response across all cases. This phenomenon was confirmed when running the exponential curve fitting algorithm to find the thermal time constants for all cases. The τ_{th} values are almost indistinguishable (less than a millisecond difference) around 37.5 ms; this is indicated by the vertical dashed line on the plot. Figure 18(b) shows the response for the maximum value of Cr responsivity while SiN_x emissivity is varied from 0.5 to 0.9. Again, while the thermal time constant is indistinguishable among the transient responses, the final value of responsivity is within 10mK/μW difference.

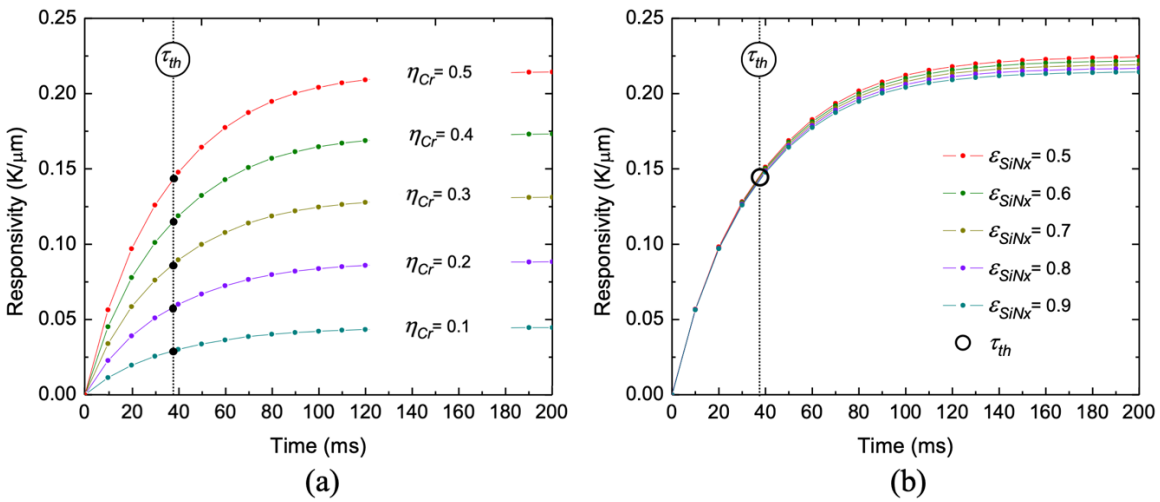

Transient response of THz-to-IR sensor when (a) SiN_x emissivity is constant at 0.9 at desired LWIR band. (b) Cr absorptivity constant at 0.5. Thermal time constant was evaluated and is indistinguishable for all cases.

Figure 18. Transient Response – (a) SiN_x Emissivity Constant; (b) Cr Absorptivity Constant

It is important to observe that the thermal time constant does not change for all tested combinations. Although 30 ms allows for real time imaging (~30 frames per

second), the sensor configuration or geometry must change if the application requires faster operation. The first variable to change is to reduce the thermal insulation of the sensing element. This insulation reduction can be accomplished by an increase in thermal conduction on the insulating beams. Recall Equation (3) where the thermal conduction is directly proportional to the cross-sectional area, A_c of the beam. A_c in Equation (3) is equal to $l_w \times t_{diel}$ in Figure 7. If the beam width (l_w) is increased, more heat will transfer to the heat sink making the sensor faster. As previously discussed, the tradeoff at this point will be the reduction of responsivity. The other option is to make the dielectric layer thinner to reduce thermal mass. This option requires several runs of fabrication and structural tests in follow work. The team will then need to see if a thinner sensing element would survive structurally while exhibiting similar radiation properties.

While the change in SiN_x emissivity has a small effect on responsivity, its impact should be viewed in terms of SR_{eff}. The higher the emissivity, the higher the radiant flux change due to ΔT that is transferred to the readout IR camera. To evaluate the sensor SR_{eff} we start with the ideal case where the layer properties are represented in Figure 9. Using Equation (9) with the ideal case properties, we obtain a SR_{eff} of 0.96. This will never be unity because there will always be some radiation from the front side. The efficiencies for all cases of Figure 16 were evaluated for Cr absorptivity at its maximum (0.5) and for an incident power of 1 μW. Table 1 lists a summary of the used quantities and the results.

Table 1. Efficiency Evaluation of Figure 16 Sensor Configurations

ε_{SiNx}	BB	0.5	0.6	0.7	0.8	0.9	ideal
ΔT (K)	0.21	0.231	0.229	0.228	0.227	0.225	0.235
SR_{eff}	0.35	0.34	0.39	0.42	0.46	0.49	0.96

Cr absorptivity kept constant at 0.5, incident power of 1μW.

From the data in Table 1, it is clear that as the emissivity of the SiN_x layer increases, the efficiency increases and consequently the heat flux radiated from the sensor backside (towards the COTS IR camera). The efficiency of the BB case is lower since the sensor is radiating over the entire spectrum from both sides with maximum emissivities.

It is important to highlight that for small temperature variations such as the ones experienced for low incident power levels (realistic), the efficiency is independent of ΔT. The most impacting factors are the SiN_x emissivity selectivity and magnitude; we can compare all cases with the BB case here.

Upon review of this analysis, the target for the sensor layers would be to achieve the maximum absorptivity for the Cr film and the maximum LWIR selective (7–14μm) emissivity for the SiN_x layer. Based on the capabilities of NPS's microfabrication facilities along with results obtained in previous works [6], [9] we can come to some labeled goals. A sensor with an evaporated nanoscale Cr film with absorptivity close to 0.5, and a LWIR selective-emissive SiN_x layer with emissivity close to 0.9 (deposited using PECVD), is likely to be achieved.

THIS PAGE INTENTIONALLY LEFT BLANK

IV. FABRICATION AND CHARACTERIZATION

The fabrication and characterization methods discussed in this chapter are the results of collaboration among our team members and their still unpublished work. Specifically, the author would like to credit Mr. Ricky Lee, a researcher within the NPS Physics Department Photonics Lab for his aid and notes in the completion of this chapter.

The fabrication process suggested in this chapter was developed based on the NPS microfabrication facility (class 1000 clean room) capabilities. Several results obtained by testing the processes at NPS and Center for Nanophase Materials Sciences (CNMS) at the Oak Ridge National Laboratory also contributed to our fabrication process.

Initially, films of SiN_x and Cr were deposited on undoped 4" Si substrates to allow characterization and tuning of the deposition processes. The dielectric layer was deposited first using an Oxford Instruments Plasmalab System (Oxford 100), running a PECVD process. The inductively coupled plasma power was set at 500 W while experiencing a chamber pressure of 10.0 mTorr. The Silane (SiH_4) was diluted on N_2 at a rate of 1:99. The SiH_4 and Argon (Ar) were set to flow at 50.0 sccm and 15.0 sccm, respectively while the substrate was kept at 300º C. The thicknesses of the films after a few trials were measured using an optical interferometer (Filmetrics F-40 Film Thickness Measurement Tool); films between 800 and 1600 nm were obtained. The spectral response of the fabricated sample was measured in a Thermo-Nicolet Nexus 870 Fourier Transform Infrared Spectrometer (FTIR) fitted with a globar source, a PIKE Technologies MappIR accessory, a Si beam splitter, and a pyroelectric detector [10]. In order to obtain absorptivity, measurements of specular reflectivity and transmissivity were performed. Since the films are homogeneous, second order scattering can be neglected and absorptivity is simply obtained by Equation (13).

$$Abs = 1 - (Refl + Trans). \qquad (13)$$

Figure 19 (a) and (b) shows schematic representations of the setup. The measurements were taken at off-normal incidence (15°) due to the optical arrangement of the FTIR accessory. For the background subtraction a 300 um Si wafer (from the same lot

as the substrate where the SiN_x was deposited initially) was used on top of a gold mirror for reflectivity and on the beam path for transmissivity. With this arrangement, only the SiN_x optical properties were observed.

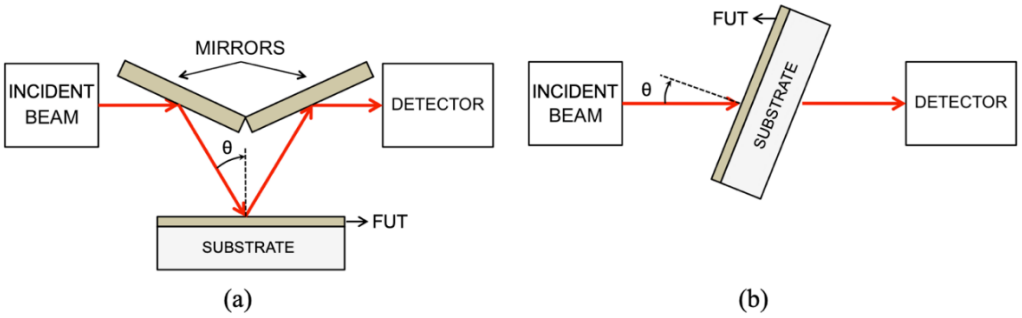

Figure 19. Schematic Representation of (a) Reflectivity and (b) Transmissivity Measurement Configurations. FUT – Film Under Test

Figure 20 shows the absorptivity of three SiN_x films from 2 to 55 THz, which correspond to wavelengths of 150 to 5.5 μm. Note the evident selectivity and higher emissivity shown between 20 to 40 THz of the 800 nm film.

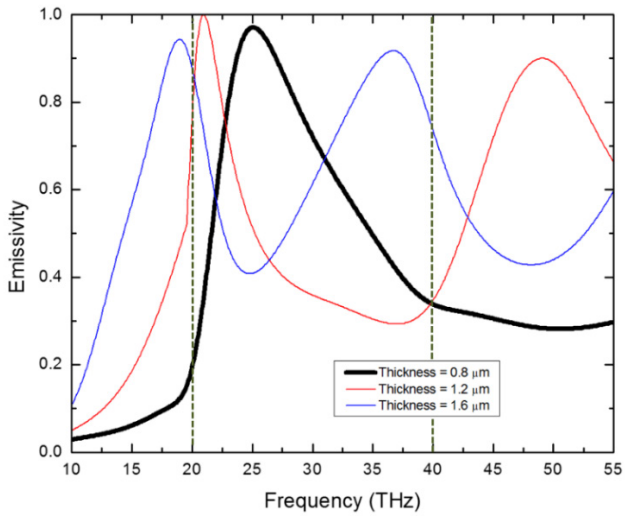

Emissivity of SiN_x films measured using a FTIR. Note that the 800 nm film exhibits the best selectivity in the targeted range (20–40 THz).

Figure 20. PECVD Deposited SiN_x Emissivity

Nanoscale Cr films were deposited on top of the SiNx layer, with the goal being to obtain the thinnest possible film exhibiting the highest absorptivity. Therefore, the conductivity of the film was estimated to be 5×10^5 S/m (see figure (b)). Several attempts were made using an Angstrom Engineering Covap metal evaporator; here a Cr target in a vacuum chamber (~ 10–^{6} Torr) is heated by current flow and the vapor is deposited on the rotating substrate placed above the target. After deposition, the thickness of the film was measured with the following two methods; contact profilometry (via KLA Tecnor Contact Profilometer) and FILMEX interferometer (same used for the SiN_x films). Conductivity of the film was measured on a 4-point probe (Pro4 4-Point Resistivity Measurement System). Cr deposition using the metal evaporator was not successful due to target degradation. Several films were deposited and an extremely poor conductivity was obtained for thin films (~10–50 nm); consequently, the THz absorptivity of those films would also be very low. Other attempts were made using a sputtering instrument (Angstrom Covap Metal Evaporator), and better conductivity was obtained. However, due to a relatively low vacuum held during deposition (inherent limitation of the instrument), the films became oxidized and the ideal conductivities were not achieved. The best result was a 14 nm film with $3.9\text{x}10^5$ S/m. Figure 21 shows the measurement, performed exactly in the same way as for the SiN_x films. While this film gives THz absorptivity around 0.25, half of the desired value, it is still important as it fits well in Equation (8).

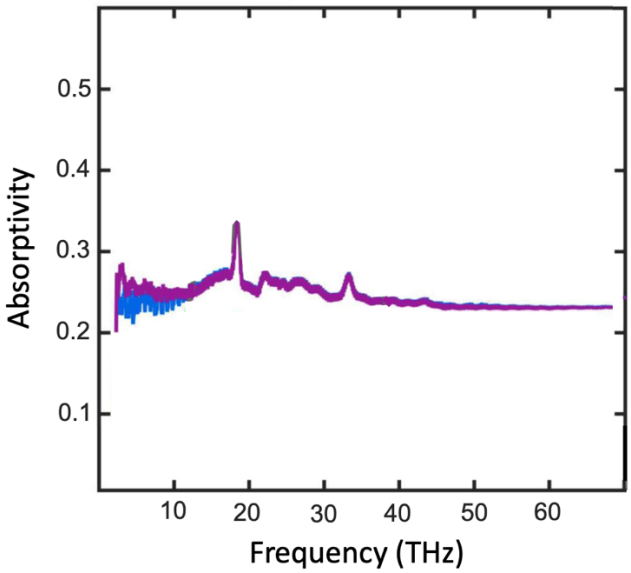

Absorptivity of a Cr thin film measured using a FTIR. Data was extracted manually (blue line) and via FTIR software (purple line). The peaks between 20 and 35 THz are artifacts of the measurement.

Figure 21. Sputter Deposited Cr Absorptivity

The ripple shown between 0.5 and 10 THz is due to multiple reelections on the substrate (i.e., the Fabry-Perot effect). The absorption of the metallic film was demonstrated to be the top envelope of the ripple [6]. The deficiencies of the Cr deposition procedure are in the process of being corrected; currently, NPS is acquiring a new high performance sputter machine. Additionally, through a partnership with the CNMS, electron beam evaporation will be used to optimize the Cr films. This was performed in the past using CNMS's equipment with outstanding results [6], as depicted in Figure 8.

Once the functional materials are optically characterized, the fabrication processes and sequence to fabricate the FPA must be established. The configuration of the sensors to be fabricated is shown in Figure 6. In order to manufacture the sensor, a photolithographic process is used to transfer the patterns to be etched to the surface of the materials. Photomasks, made of soda-lime glass with a Cr layer containing the pattern to be transferred, are produced by industrial partners. The masks are designed using the layout tool L-EDIT^{TM}, from the MEMSPro software licensed to NPS. To assure that the

fabrication process is providing the desired results and to test the material properties after fabrication, auxiliary structures are placed in the wafer to be inspected and measured during different phases of the process. Figure 22 shows the combined layout of the three photomasks used for this project. All features on the masks are commented in the figure and fit inside a 4-inch substrate.

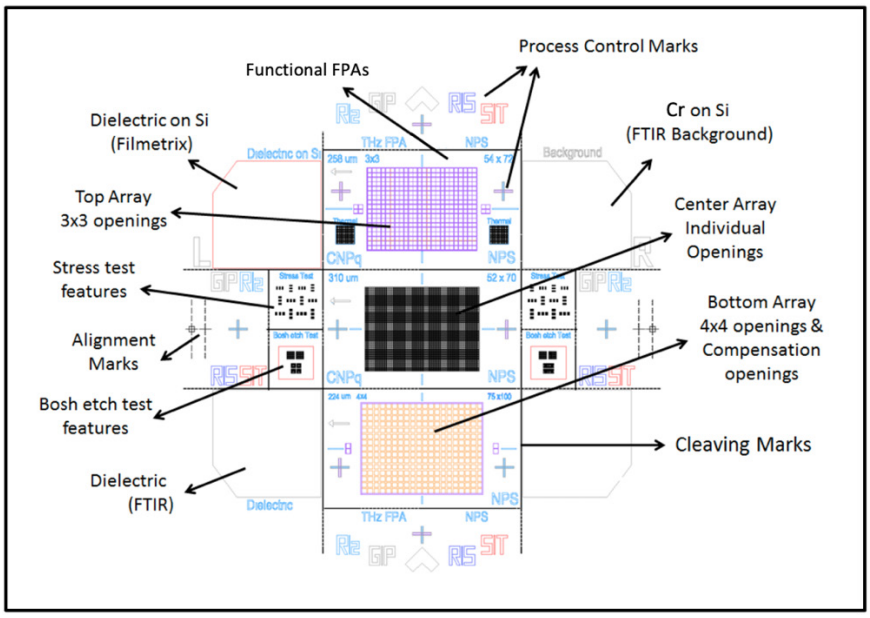

Figure 22. Visualization of Three Photomasks for Fabrication

Note the small features not shown in this scale are evident in Figure 23 where the process sequence is illustrated. The three large rectangles in the center of Figure 22 are arrays of sensors with slightly different features such as backside openings, metallic frames around the pixel and other minor additions to allow tuning of the process. The corners of all quadrants are reserved for homogeneous layers of the constituent materials. These corners are used post-fabrication to measure the actual absorptivity and emissivity of Cr and SiN_x on the sensors. Other features are stress test structures, process control lines and cleaving marks (for dicing of the functional arrays). Important features to note that are symmetrically located on both sides of the mask are the alignment marks, which are specially designed to allow precise alignment between the masks and the processed

wafer. Figure 23 shows the fabrication sequence of a single pixel (center array on Figure 22), visualized using MEMSPro™.

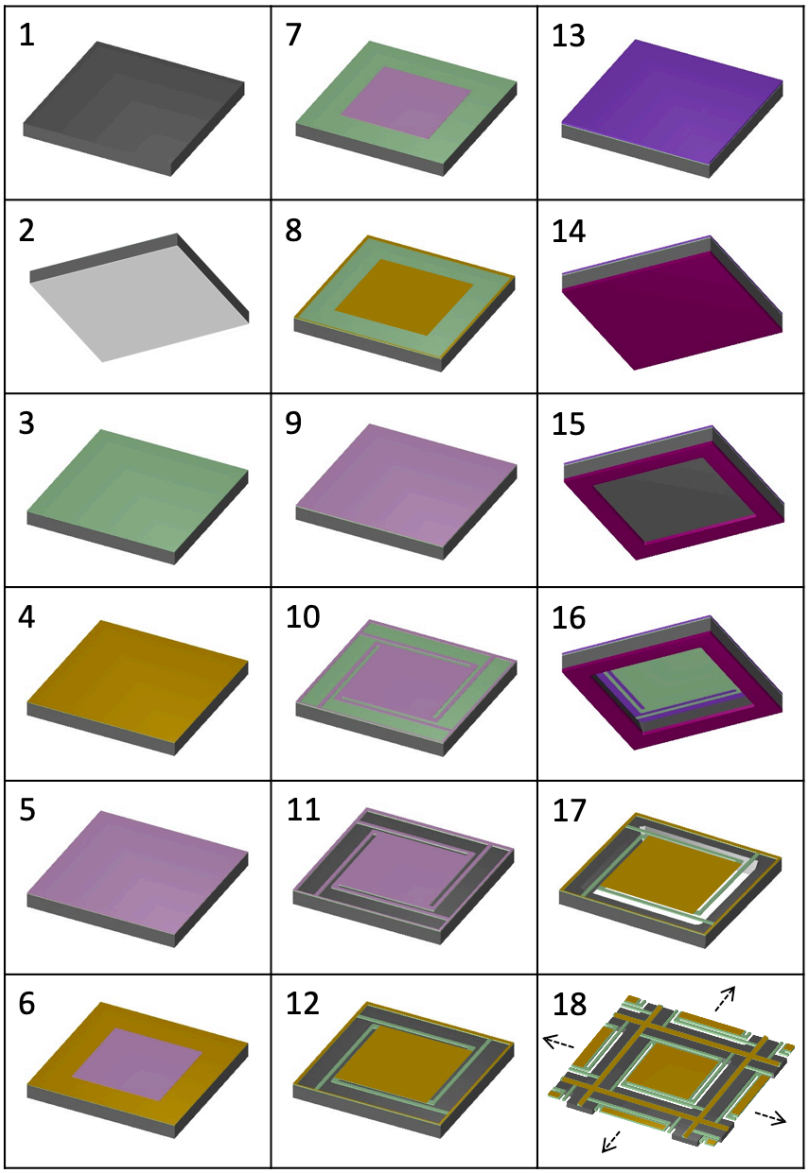

Figure 23. Single Pixel Microfabrication Sequence Visualized in MEMSPro L-Edit™

The fabrication steps depicted in Figure 23 are described as follows:

1. The substrate, 4-inch P-doped (10-20 Ωcm resistivity), 1–0-0 oriented, double side polished Si wafer 300 μm thick, is inspected and cleaned on oxygen plasma for 5 minutes. This process removes all organic contaminants and prepares the substrate surfaces for the subsequent processes.

2. A layer of 100 nm Aluminum (Al) is deposited on the back side of the substrate using thermal evaporation similar to the Cr deposition. The difference here is that the Al target is comprised of solid pellets placed on a resistive boat where high current passes through. The Al is allowed to melt and soak for homogenization before higher current is applied and the evaporation starts. This layer serves as an extra mask for Step (16) where the substrate is completely removed/etched from the back side.

3. An 800 nm thick SiN_x film is deposited on the top side of the substrate. The PECVD deposition process is exactly the same as described earlier.

4. A 10 nm Cr layer is deposited on top of the SiN_x layer as previously described.

5. SPR 955–0.7 photoresist is spun over the top at 3000 RPM for 45 seconds ramped and then soft baked (pre-exposure) for 90 seconds at 115^o C.

6. The photoresist is UV exposed for 2 seconds in the EVG 620 contact aligner, where the first mask (sensing element) containing the Cr sensing element pattern is transferred to the resist. The wafer is soaked in CD26 for 20 seconds with agitation and the UV exposed resist is dissolved. The wafer is cleaned in deionized water and dried with 99.99% pure Nitrogen (GN2).

7. The unmasked Cr is removed using Ar sputter etch on the Oxford 100. This step is very critical since only 10 nm of Cr should be removed and the SiN_x layer underneath it should be mostly untouched; the process lasts about 15 seconds. Another procedure is the wet etch of Cr using Cr

etchant. Soaking the wafer on Cr etchant for approximately 20 seconds should be enough.

8. The remaining photoresist is removed in an acetone bath for approximately 5 minutes. The thickness of the step at the edge of the Cr square is measured to assure the Cr was completely removed. In addition, the thickness of the remaining SiN_x layer is measured in the Filmetrix equipment to assure over-etch does not compromise structural integrity.

9. Another layer of SPR 955–0.7 photoresist is spun using the same process described in Step (5).

10. Step (6) is repeated here, but with the second mask (sensor structure).

11. Ar sputter etch is completed for 45 seconds on the Oxford 100. This removes the unmasked SiN_x, exposing the underlying pixel structure.

12. Step (8) is repeated. The over-etch due to Ar sputtering is negligible since whatever Si remaining will be removed from the backside in Step (16).

13. A thick photoresist layer is applied to the top of the wafer to protect the structures. This is necessary because the wafer will be flipped for the backside process. SPR 220–7 is spun at 3000 RPM for 45 sec and baked at 90º C for 4 hours in order to cure. This should provide a hard protective layer of about 7 μm. The wafer can then be processed from the backside without compromising the front side structures.

14. The same photoresist is spun on the backside of the wafer then baked at 115º C for 90 seconds. This provides an extra 7 μm layer mask on top of the Al layer.

15. The photoresist is UV exposed for 6 seconds in the contact aligner where the third mask (backside opening) is transferred to the resist. The wafer is

soaked in CD26 (30 seconds with agitation) and the UV exposed resist is dissolved.

16. This step is divided into two parts. Initially, Al wet etch is performed to remove the unmasked Al. The wafer is soaked for 50 seconds in Al etchant and cleaned with deionized water and isopropanol. Next the wafer is placed in the Oxford 100 where deep Si etch is performed to remove the unmasked Si. This deep etch requires about 400 double-cycles of a process called Bosh etching [1] to go through the entire Si thickness and stop on the top side of the SiN_x. Careful tuning and adjustment of parameters is required and will be studied and evaluated in future work.

17. All remaining photoresist is removed in oxygen plasma for about 5 minutes, releasing the sensing elements and the thermal insulating beams.

18. A partial view of the side pixels is shown to reinforce that all these steps are carried out on the entire wafer. The FPA as well as all other structures are fabricated simultaneously.

Figure 24 shows an actual wafer with the structures from mask 1 and 2 transferred to it. Steps (1)-(12) (Figure 23) were successfully performed on a 300 μm thick, 4-inch Si substrate. The remaining steps were not performed and will be a topic for future work.

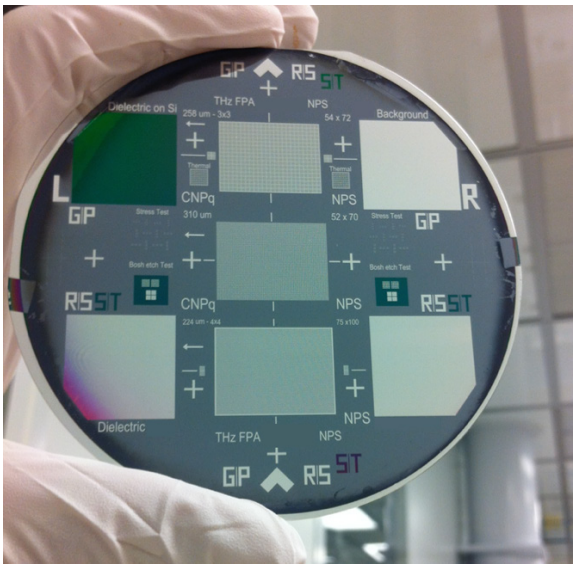

Figure 24. Photo of 4-inch Si Wafer With Steps (1)-(12) Performed

V. CONCLUSION

The objective of this thesis was to design a MEMS-based broadband THz-to-IR converter FPA using nanoscale metal films with dielectric thin film structures for potential space operation. This FPA is to be fitted with THz focusing optics and a COTS LWIR camera to be placed in a CubeSat with the aid of the NPS SSAG for launch into LEO.

In order to achieve this objective a study of thermal sensors and their main figures of merit that translate to band converters was performed. The important characteristics of THz broadband absorption and IR radiative emission were identified and design criteria were established. A sensor configuration was suggested based on legacy experience of our research group as well as existing capabilities of NPS's microfabrication facilities. Responsivity, thermal time constant, and selective radiation efficiency were defined for the MEMS band converter to provide a means of design, analysis, and performance comparison. A FE analysis model was developed in COMSOL aided with post-processing performed in Matlab to estimate the figures of merit. Chromium nanoscale films and silicon nitrate thin films were selected as the THz absorber and the IR emitter, respectively. These constituent materials were chosen based on their optical and structural properties.

A thorough analysis of the impact of the metal and dielectric films' optical properties on the figures of merit was conducted. The temperature swing that could be experienced by the sensor during LEO were also considered in the FE analysis simulations. Configurations where the front side of the sensor exhibits a broadband THz absorptivity (0.5–10 THz), and the backside of the sensor exhibits a selective emissivity in the band of the COTS LWIR camera used as a readout were considered. The main outcomes of this analysis for a nanoscale Cr film (5 - 50 nm) was that the maximum absorption of 0.5 is achievable, whereas for a SiN_x thin film, selective emissivities between 0.5 and 0.9 can be obtained. While the absorptivity of Cr wields great impact on responsivity, the thermal time constant remained unchanged around 30 ms. Increasing the emissivity of the SiN_x layer slightly reduces the responsivity, however it significantly

increases the radiation efficiency, important for the IR readout. In addition, responsivity was found to be temperature dependent; therefore, calibration curves must be applied when the sensor is deployed.

The requirements for an ideal band converter were slightly compromised by their feasibility. Therefore, a realistic configuration using 10 nm of Cr (absorptivity = 0.5) and 800 nm of SiNx (selective emissivity = 0.9) was suggested to be fabricated to its highest efficiency (~ 0.5).

Several samples of Cr and SiN_x films were deposited onto Si substrates and their characteristics were measured. While good results were obtained for PECVD deposited SiN_x films, the evaporation process of Cr was compromised by the limitations of the available tools. The nitrate film of 800 nm showed selective response in the desired range and we believe 800 nm is still a suitable thickness for structural concerns. The Cr deposition deficiencies are going to be addressed in future work by using different tools in different partner laboratories.

A detailed process to fabricate the THz-to-IR FPA was studied and simulated using MEMSPro^{TM}; consequently an optimal sequence/recipe was identified and suggested. This “recipe” includes photolithographic masks organization and layout, tooling parameters, deposition, etching and cleaning procedures. Fabrication of the FPAs was performed partially to the point where deep Si etch of the backside is needed to conclude the first samples. This is a task for future work.

Although the objective of this research was fully achieved, there is much to be done to have a space-deployable THz-to-IR imager assembly. The limitations in Cr deposition must be addressed to allow maximum performance. The FPA fabrication process must be finished and tuned to be repeatable and portable, which may require fabrication to potentially be conducted in other facilities other than NPS. Additionally, full characterization must be performed in a laboratory setting using available THz sources. Calibration curves must be obtained to compensate for the temperature swing the sensor will experience in LEO. THz and IR dedicated optics must be designed and integrated into the assembly to allow for THz imaging.

With the development of new compact and powerful THz sources such as quantum cascade lasers, this THz-to-IR band converter can have its applications, both on-orbit and terrestrial, expanded significantly. The simplicity of the device allows it to be used as an attachment to any COTS LWIR camera. This “attachability” can be used for non-invasive inspections of military assets, real time security screening, and/or packaging inspection—replacing much more expensive equipment currently in use.

THIS PAGE INTENTIONALLY LEFT BLANK

APPENDIX A. ADDITIONAL FIGURES

The collection of graphs shown in this Appendix correspond to data extracted from COMSOL simulations and post processed using Matlab routines. The thermal time constant was obtained using an exponential fitting routine developed by the author. The parameters and simulation conditions are described on the figure captions.

Initially, in order to observe how the figures of merit change with absorptivity (η_{THz}) and emissivity (ε_{SiNx}) of the front and backside, respectively, it was assumed that the sensor had no selectivity (η_{THz} and ε_{SiNx} constant over all electromagnetic spectrum). In addition, the absorbed power, ΔP_0 (which is the incident power, ΔP weighed by the Cr layer absorptivity, η_{THz}) was kept constant at 1μW.

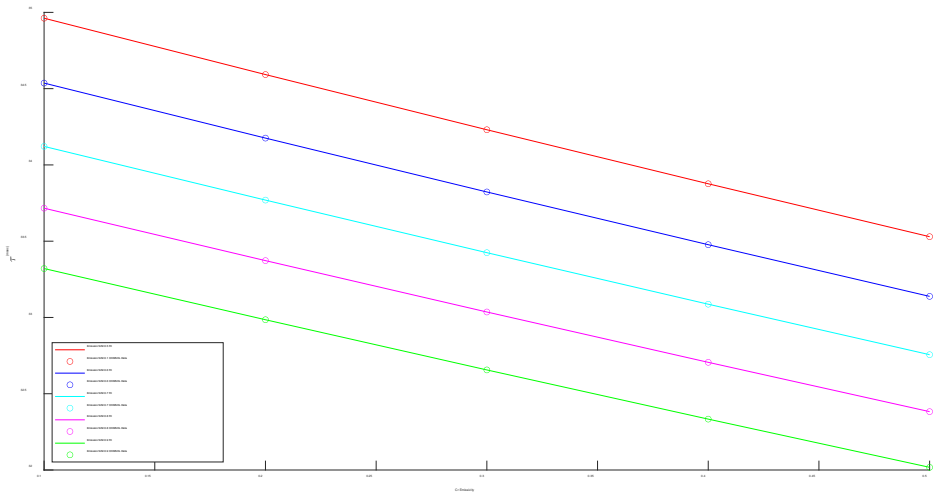

Figure A1. τ_{th} - Absorbed Power 1 μW at 20º C Ambient Temperature

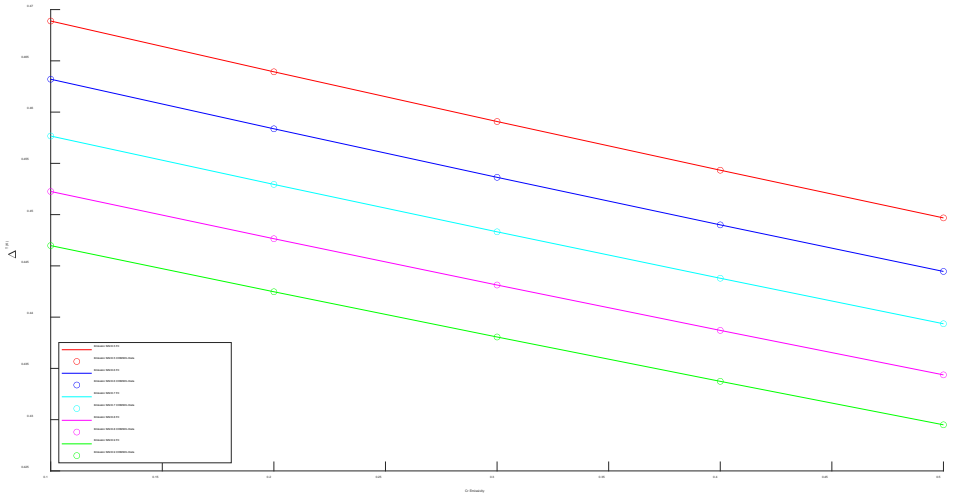

Figure A2. ΔT - Absorbed Power 1 µW at 20° C Ambient Temperature

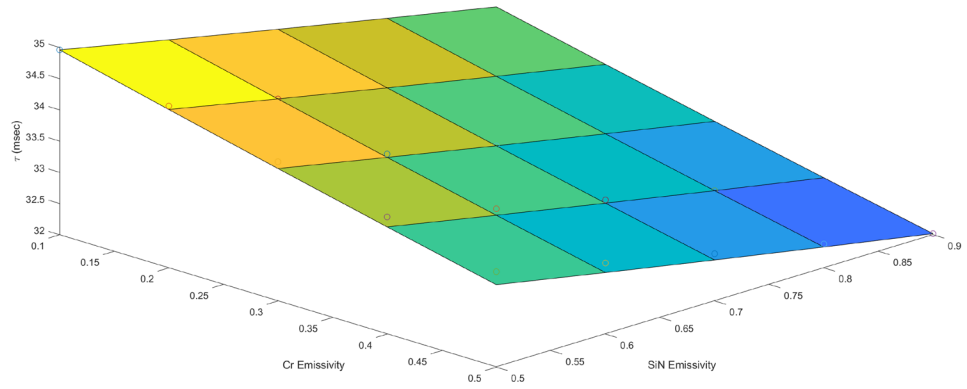

Figure A3. Figure A1 in 3D

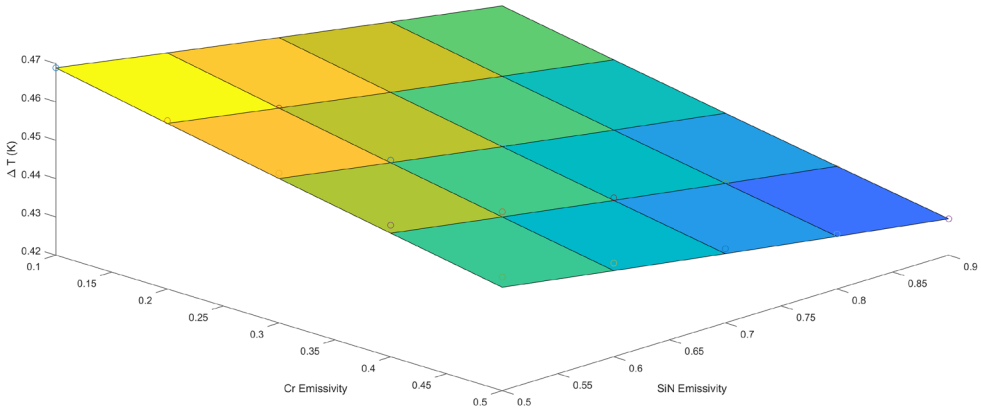

Figure A4. Figure A2 in 3D

From now on, the figures shown correspond to simulations where the incident power (ΔP) is kept constant at 1μW, therefore the absorbed power is proportional to the absorptivity of the Cr layer (realistic case). In addition, ambient operating temperatures of the spacecraft corresponding to the extremes of those experienced in LEO are also considered.

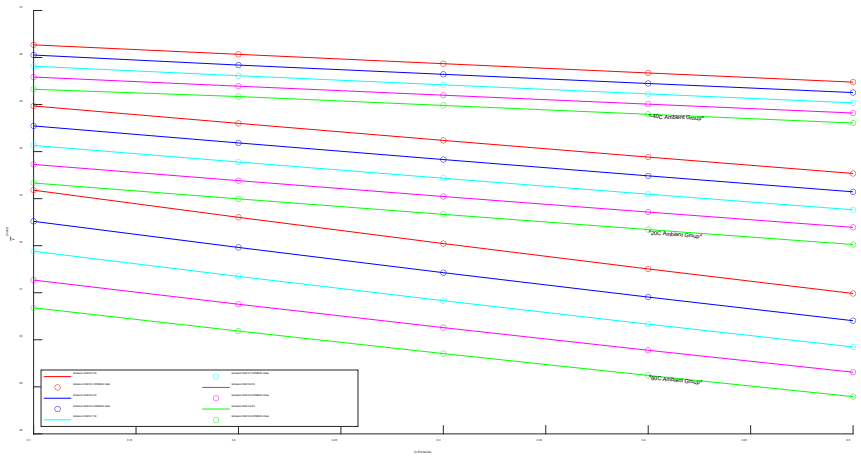

Figure A5. τ_{th} - Incident Power 1μW at -40° C, 20° C, 80 ° C Ambient Temperatures.

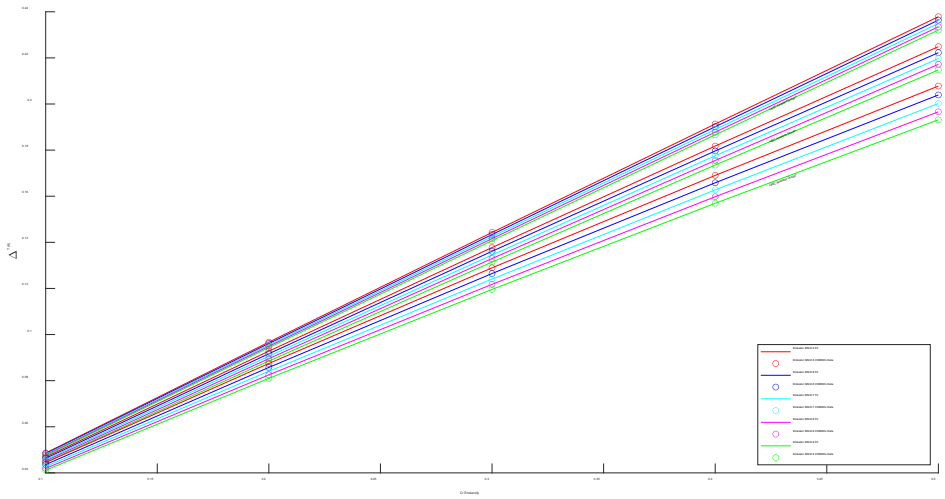

Figure A6. ΔT - Incident Power 1μW at -40° C, 20° C, 80 ° C Ambient Temperatures.

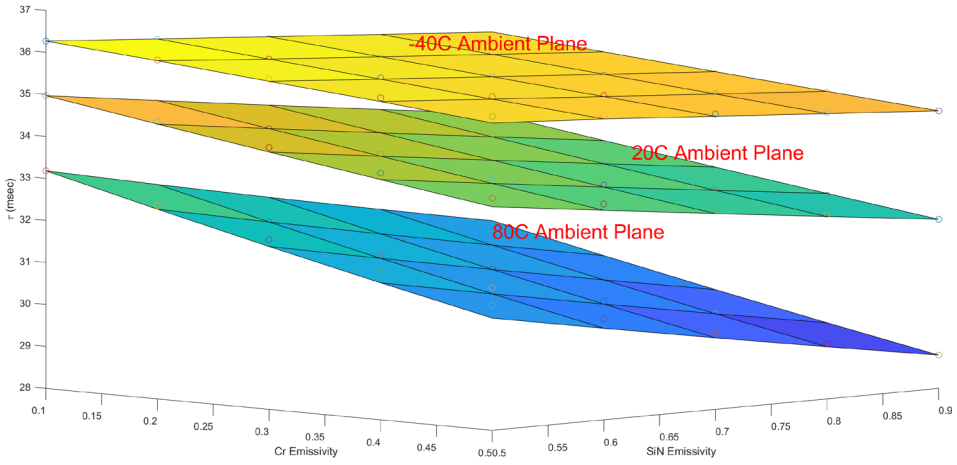

Figure A7. Figure A5 in 3D

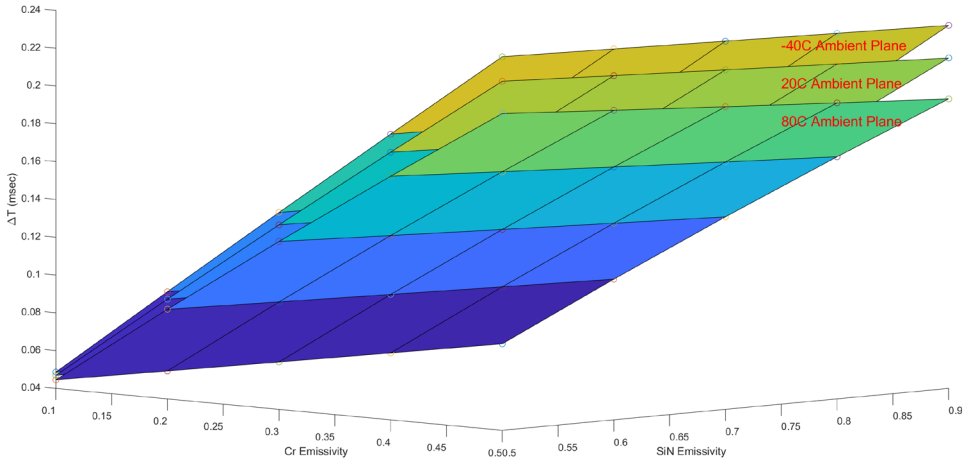

Figure A8. Figure A6 in 3D

THIS PAGE INTENTIONALLY LEFT BLANK

APPENDIX B. EXPONENTIAL CURVE-FIT ALGORITHM MATLAB CODE

```
%% Thesis Matlab File 1
% LT Anish H Bhatt
% Thermal Time Constant Calculation and Validation
% NOTE: Save "TimeDomainData.xlsx" and "1_00HzDataVersion3.csv" in the same
% folder as this matlab "TimeConstantCalculation.m" file.

%Step 1: plot 1Hz gate frequency in COMSOL, up to 0.50000 seconds exactly
%Step 2: put this data into table format, export in excel table format

%% RMS Frequency and Thermal Time Constant Calculation - Method 1 (Long)
clc
clear all
close all

%Read in excel data6
%Normalized over the 1Hz Max Temp because this is assumed to be the steady
%state temperature assuming an infinitely long application of the laser
DeltaT_Normalized=xlsread('TimeDomainData.xlsx',1,'J2:J20');
GateFreq=xlsread('TimeDomainData.xlsx',1,'E2:E20'); %Hz

%Interpolate to find PRECISE frequency
RMSFreq_Hz=interp1(DeltaT_Normalized,GateFreq,sqrt(2)/2,'pchip');
TimeConstant_sec=1/(2*pi*RMSFreq_Hz);
TimeConstant_msec_Method1=TimeConstant_sec*1000

%Plot
loglog(GateFreq,DeltaT_Normalized)
%title('Normalized Steady \DeltaT (After 1 Second) As Function of Gate Frequency')
xlabel('Gate Frequency (Hz)','FontSize',20)
ylabel('\DeltaT (Normalized Over 1Hz Max Temp)','FontSize',20)
set(gca,'FontSize',20)
xlim([min(GateFreq) max(GateFreq)])
hold on;
plot(RMSFreq_Hz,sqrt(2)/2,'r*')
hold on;
plot([RMSFreq_Hz RMSFreq_Hz],[min(DeltaT_Normalized) sqrt(2)/2],'r--')
plot([min(GateFreq) RMSFreq_Hz],[sqrt(2)/2 sqrt(2)/2],'r--')
string=['f_o = ',num2str(RMSFreq_Hz),' Hz'];
text(RMSFreq_Hz+1,sqrt(2)/2,string,'FontSize',20)

%% RMS Frequency and Thermal Time Constant Calculation - Method 2 (Short)
```

```
clear all
format long

%Read in excel data for gate frequency 8.76 Hz (8.7569 Hz was the RMS Freq)
time=xlsread('1_00HzDataVersion3.csv',1,'B6:B505'); %sec
Temp=xlsread('1_00HzDataVersion3.csv',1,'C6:C505'); %K

%Plot
figure(2)
plot(time,Temp,'ro')
%%%%%%%%%%%%%%%%%%%%%%%%%%%%%%%%%%%%%%%%%%%%%%%%%%%%%%%%%%%%%%%%%%%%%%%
%%%%%%%%%%%%%%%%%%%%%%%%%%%%%%%%%%%%%%%%%%%%%%%%%%%%%%%%%%%%%%%%%%%%%%%
%SPECIFIC ALGORITHM PUT TOGETHER BY ANISH AFTER RESEARCH
ONLINE FOR BEST
%CURVE FIT OPTIONS...
f=@(b,time) b(1).*exp(b(2).*time)+b(3); %Objective Function
B=fminsearch(@(b) norm(Temp - f(b,time)), [-2000; -1; 3000]); %Estimate Parameters
%%%%%%%%%%%%%%%%%%%%%%%%%%%%%%%%%%%%%%%%%%%%%%%%%%%%%%%%%%%%%%%%%%%%%%%
%%%%%%%%%%%%%%%%%%%%%%%%%%%%%%%%%%%%%%%%%%%%%%%%%%%%%%%%%%%%%%%%%%%%%%%
hold on
plot(time, f(B,time), '-b','LineWidth',2) %PLOT THE CURVE FIT
xlabel('Time (sec)')
ylabel('Temperature (K)')
title('1.00 Hz Gate Frequency Temperature vs Time (Temp Rise Half Cycle Only)')
legend('1Hz COMSOL DATA','Matlab Exponential Curve Fit','Location','SouthEast')
text(.2, 293.55, sprintf('f(x) = %.1f\\cdote^{%.3f\\cdotx}%+.1f', B)) %OUTPUT THE
CURVEFIT EQUATION ON THE PLOT
TimeConstant_msec_Method2=1000*(1/abs(B(2))) %The thermal time constant is the
inverse of the exponent coefficient
```

LIST OF REFERENCES

[1] F. Alves, L. Pimental, D. Grbovic, and G. Karunasiri, "MEMS Terahertz-to-Infrared band converter using frequency selective planar metamaterial," *Sci. Rep.*, vol. 8, no. 1, p. 14, Dec. 2018. [Online]. doi: https://doi.org/10.1038/s41598-018-30858-z

[2] L. E. Pimental, "Metasurface-Based MEMS Thz-to-IR focal plane array," M.S. thesis, Dept. of Appl. Phys., NPS, Monterey, CA, USA, 2019. [Online]. Available: http://hdl.handle.net/10945/60448

[3] K. J. Weatherill, "Full-field Terahertz imaging at Kilohertz frame rates using atomic vapor," *Phys. Rev. X*, vol. 10, no. 1, p. 011027, Feb. 2020. [Online]. doi: https://doi.org/10.1103/PhysRevX.10.011027

[4] "Terahertz Technology," Terahertz (THz) technology and science | TeraSense. [Online]. Available: https://terasense.com/terahertz-technology/

[5] B. N. Behnken, "Real-time Terahertz imaging using a quantum cascade laser and uncooled microbolometer focal plane array," Ph.D. dissertation, Dept. of Appl. Phys., NPS, Monterey, CA, USA, 2008. [Online]. Available: http://hdl.handle.net/10945/10329

[6] F. Alves, A. Karamitros, D. Grbovic, B. Kearney, and G. Karunasiri, "Highly absorbing nano-scale metal films for terahertz applications," *Opt. Eng.*, vol. 51, no. 6, p. 063801, May. 2012. [Online]. doi: https://doi.org/10.1117/1.OE.51.6.063801

[7] V. M. Muravev, P. A. Gusikhin, I. V. Andreev, and I. V. Kukushkin, "Novel relativistic plasma excitations in a gated two-dimensional electron system," *Phys. Rev. Lett.*, vol. 114, no. 10, p. 106805, Mar. 2015. [Online]. doi: https://doi.org/10.1103/PhysRevLett.114.106805

[8] F. Alves, D. Grbovic, B. Kearney, N. V. Lavrik, and G. Karunasiri, "Bi-material terahertz sensors using metamaterial structures," *Opt. Express*, vol. 21, no. 11, p. 13256, Jun. 2013. [Online]. doi: https://doi.org/10.1364/OE.21.013256

[9] S. Lee, "SiN_x/Al Metamaterial-Based Terahertrz-to-Infrared converter for real-time imaging," M.S. thesis, Dept. of Appl. Phys., NPS, Monterey, CA, USA, 2019. [Online]. Available: http://hdl.handle.net/10945/62811

[10] F. Alves, D. Grbovic, J. Arruda, R. Santos, and G. Karunasiri, "Improving sensitivity and defying residual stress in MEMS bi-material Terahertz sensors with metamaterial structures and self-leveling configuration," in *8th International Congress on Advanced Electromagnetic Materials in Microwaves and Optics*, Denmark, Aug. 2014. [Online]. doi: 10.1109/MetaMaterials.2014.6948615

[11] G. Kirchhoff, "On the relation between the radiating and absorbing powers of different bodies for light and heat," *Lond. Edinb. Dublin Philos. Mag. J. Sci.*, vol. 20, no. 130, pp. 1–21, Jul. 1860. [Online]. doi: https://doi.org/10.1080/14786446008642901

[12] F. Alves, B. Kearney, D. Grbovic, and G. Karunasiri, "Narrowband Terahertz emitters using metamaterial films," *Opt. Express*, vol. 20, no. 19, p. 21025, Sep. 2012. [Online]. doi: https://doi.org/10.1364/OE.20.021025

[13] F. Alves, B. Kearney, D. Grbovic, N. V. Lavrik, and G. Karunasiri, "Strong Terahertz absorption using SiO_2 /Al based metamaterial structures," *Appl. Phys. Lett.*, vol. 100, no. 11, p. 111104, Mar. 2012. [Online]. doi: https://doi.org/10.1063/1.3693407

[14] C. J. Willers, *Electro-Optical System Analysis and Design: A Radiometry Perspective*. Bellingham, WA, USA: Society of Photo-Optical Instrumentation Engineers, 2013.

[15] J. A. Kozak, "Testing, integration, and concept of operations development for a Thz imaging camera payload," M.S. thesis, Space Systems Academic Group, NPS, Monterey, CA, USA, 2019.

INITIAL DISTRIBUTION LIST

1. Defense Technical Information Center
   Ft. Belvoir, Virginia

2. Dudley Knox Library
   Naval Postgraduate School
   Monterey, California